Kinematics and wake of freely falling cylinders at moderate Reynolds numbers

Clément Toupoint, Patricia Ern, Véronique Roig

Kinematics and wake of freely falling cylinders at moderate Reynolds numbers

Clément Toupoint[1,2], Patricia Ern[2,†] and Véronique Roig[2]

[1]IFP Energies Nouvelles, Rond-point de l'échangeur de Solaize, BP 3, 69360 Solaize, France
[2]Institut de Mécanique des Fluides de Toulouse (IMFT), Université de Toulouse, CNRS, 31400 Toulouse, France

We investigated experimentally the motion of elongated finite-length cylinders (length L, diameter d) freely falling under the effect of buoyancy in a low-viscosity fluid otherwise at rest. For cylinders with densities ρ_c close to the density ρ_f of the fluid ($\overline{\rho} = \rho_c/\rho_f \simeq 1.16$), we explored the effect of the body volume by varying the Archimedes number Ar (based on the body equivalent diameter) between 200 and 1100, as well as the effect of their length-to-diameter ratios L/d ranging from 2 to 20. A shadowgraphy technique involving two cameras mounted on a travelling cart was used to track the cylinders along their fall over a distance longer than $30L$. A dedicated image processing algorithm was further implemented to properly reconstruct the position and orientation of the cylinders in the three-dimensional space. In the range of parameters explored, we identified three main types of paths, matching regimes known to exist for three-dimensional bodies (short-length cylinders, disks and spheres). Two of these are stationary, namely, the rectilinear motion and the large-amplitude oscillatory motion (also referred to as fluttering or zigzag motion), and their characterization is the focus of the present paper. Furthermore, in the transitional region between these two regimes, we observed irregular low-amplitude oscillatory motions, that may be assimilated to the A-regimes or quasi-vertical regimes of the literature. Flow visualization using dye released from the bodies uncovered the existence of different types of vortex shedding in the wake of the cylinders, according to the style of path. The detailed analysis of the body kinematics in the fluttering regime brought to light a series of remarkable properties. In particular, when normalized with the characteristic velocity scale $u_0 = \sqrt{(\overline{\rho}-1)gd}$ and the characteristic length scale $l_0 = \sqrt{dL}$, the mean vertical velocity $\overline{u_z}$ and the frequency f of the oscillations become almost independent of L/d and Ar. The use of the length scale l_0 and of the gravitational velocity scale to build the Strouhal number $St^* = fl_0/u_0$ allowed us to generalize to short ($0.1 \leqslant L/d \leqslant 0.5$) and elongated cylinders ($2 \leqslant L/d \leqslant 12$), the result $St^* \simeq 0.1$. An interpretation of l_0 as a characteristic length scale associated with the oscillatory recirculation thickness generated near the body ends is proposed. In addition, the rotation rate of the cylinders scales with u_0/L, for all L/d and Ar investigated. Furthermore, the phase difference between the oscillations of the velocity component u along the cylinder axis and of the inclination angle θ

† Email address for correspondence: ern@imft.fr

of the cylinder is approximately constant, whatever the elongation ratio L/d and the Archimedes number Ar.

Key words: particle/fluid flow, vortex shedding, wakes

1. Introduction

Three-dimensional bodies falling or rising under the effect of buoyancy in a fluid at rest have been a subject of continuous interest for the variety and attractiveness of the types of path that they display. Non-vertical (e.g. oblique) or non-rectilinear (e.g. periodic, chaotic, ...) paths are known to be the result of the complex coupling between the flow generated by the body motion (in particular, the wake structure) and the degrees of freedom in translation and rotation of the body. The case of the freely moving sphere illustrates the strong influence of the control parameters on the coupling between the fluid and the moving body, providing a remarkable diversity in the styles of path and associated wakes (see Auguste & Magnaudet 2018, and references therein). For this singular geometry, the control parameters are the body to fluid relative density $\overline{\rho}$, and the Archimedes number Ar comparing buoyancy and viscosity effects, defined as

$$\overline{\rho} = \frac{\rho_c}{\rho_f} \quad \text{and} \quad Ar = \left(\frac{\rho_c - \rho_f}{\rho_f} gD \right)^{1/2} \frac{D}{\nu}, \tag{1.1a,b}$$

where ρ_c is the density of the solid body, ρ_f is the fluid density, ν is the fluid kinematic viscosity, $g = 9.81$ m s^{-2} is the magnitude of the gravitational acceleration and D is a characteristic dimension of the body, the diameter in the case of a sphere. Once the mean rise/fall velocity of the body is known, a Reynolds number Re can be defined, enabling the comparison with the case of a fixed body, the corresponding velocity being then the upcoming mean flow velocity. In the case of non-spherical bodies, the anisotropy of the body has also an influence on the fluid–body coupling, by impacting the flow structure as well as the response of the body to the hydrodynamic loads. Wake instability depends on the body geometry and vortex formation is modified as soon as the symmetry axis of the body changes its orientation with respect to the body velocity. As well, non-sphericity makes anisotropic the generalized inertia tensors, involving proper and added-mass contributions, so that the ability of the body to react to hydrodynamic efforts is anisotropic. The influence of a control parameter characterizing the body non-sphericity on the properties and characteristics of the different paths, as well as on the transitions between them, is emphasized in the investigations on freely moving disks of various thickness-to-diameter ratios or two-dimensional plates of various thickness-to-width ratios (see Ern *et al.* 2012). At variance with the latter geometries, the free motion of elongated finite-length circular cylinders received until now little attention. It is however one of the simplest three-dimensional geometries, characterized by the elongation ratio, L/d, where d is the diameter and L the length of the cylinder. Moreover, this geometry aroused the surge of developments concerning wake instability and three-dimensional aspects of nominally two-dimensional wake flows about fixed cylinders (see Williamson 1996; Inoue & Sakuragi 2008) and elastically mounted cylinders undergoing vortex-induced

vibrations (see Williamson & Govardhan 2004). It is therefore the focus of the present investigation.

The problem of an infinitely long circular cylinder free to move in any direction perpendicular to its axis is a two-dimensional counterpart to the case of the sphere, and its characteristic dimension D is the cylinder diameter. To investigate the coupling between the wake instability and path oscillations, Namkoong, Yoo & Choi (2008) performed numerical simulations of the two-dimensional motion of a freely falling/rising infinitely long circular cylinder in an infinite fluid, but considered also situations of partially restrained motion in translation and rotation of the body. They focused on density ratios $0.5 < \overline{\rho} < 4$ and Reynolds numbers between 65 and 185, corresponding to an unsteady wake exhibiting periodic vortex shedding in the case of a fixed cylinder. They observed that vortex shedding induces a low-amplitude periodic motion of the cylinder, both in translation and rotation, with transverse displacements typically lower than $0.1D$ (for instance $0.08D$ for $Re \simeq 160$ and $\overline{\rho} = 1.01$). By partially restraining the cylinder translation or rotation, they further showed that the transverse motion of the cylinder delays the onset of vortex shedding, thus reducing the Strouhal number (of less than 15 %), whereas rotation has a negligible effect. A similar behaviour is found experimentally by Horowitz & Williamson (2006, 2010) for cylinders with also two degrees of freedom in translation and one in rotation, although at much higher Reynolds numbers ($3500 < Re < 7000$). For density ratios $\overline{\rho} > 0.54$, they observed small-amplitude oscillations (about $0.05D$ for $Re \simeq 3800$ and $\overline{\rho} = 2.0$), occurring at a frequency equal to the vortex shedding frequency for a stationary cylinder, and consistent with the Bénard–von Kármán vortex street observed in the wake of the body. This path was considered rectilinear by the authors owing to the negligible amplitudes involved, but also in contrast to the large-amplitude oscillatory motion observed for light cylinders ($\overline{\rho} < 0.54$). In the latter case, they recorded displacement oscillations of amplitude of the order of D in the transverse direction at a frequency approximately 1.3 times smaller (and $0.3D$ in the vertical direction at twice this frequency), in association with a wake structure comprising two vortex pairs generated per cycle. In the same configuration, Mathai *et al.* (2017) investigated numerically the effect of both $\overline{\rho}$ and $I^* = I_p/I_f$, the particle moment of inertia I_p relative to that of the fluid I_f, by varying them separately in the range [0.1, 10], thus covering heavy ($\overline{\rho} \simeq 10$) to light ($\overline{\rho} \simeq 0.1$) cylinders. They separate for $Ar \simeq 220$ (the corresponding Re is not specified) a regime of cylinder oscillation with weak to intermediate displacement amplitudes, $0 < A < 0.3D$, dominated by the effect of the parameter $\overline{\rho}$, from a regime dominated by the effect of the moment of inertia and the rotational degree of freedom, corresponding to higher amplitudes, $0.4D < A < 0.75D$. For $Ar \simeq 500$, the mass dominated regime extends until $A \simeq 0.5D$, and in the moment of inertia dominated regime, amplitudes almost double (ranging from $0.6D$ to $1.2D$) when I^* is varied. They also noted that the gradual transition from one regime to the other is accompanied by a change in the wake pattern, from the two single vortex shedding mode to the two vortex pair shedding mode identified by Horowitz & Williamson (2010). They concluded that the rotational degree of freedom can have a significant influence on the trajectories, in particular on the frequency and amplitude of the body displacement, and on the wakes of freely rising isotropic bodies.

A question that can now be asked is whether the additional degrees of freedom associated with the free ends of a finite-length cylinder would result in different paths. In other words, what would be the effect of leaving free the cylinder ends; and of allowing the six degrees of freedom of the body to be excited by the

surrounding flow structure, and to be coupled with it? Two lengths now characterize the body geometry, the diameter d and the length L. The behaviour of circular cylinders of finite span-length moving through still water by buoyancy was studied by Marchildon, Clamen & Gauvin (1964) for $70 < Re < 2400$ (Re is based on d) and $1.46 < L/d < 35$, and by Chow & Adams (2011) for $200 < Re < 6000$ and $1 \leqslant L/d \leqslant 90$, in both cases for a wide range of cylinder materials and therefore densities, ranging from wood ($\rho_c = 0.74$ g cm^{-3}) to gold alloy ($\rho_c = 11.7$ g cm^{-3}). For these extensive ranges of parameters, both studies record a periodic motion of the cylinder consisting of an angular oscillation of the symmetry axis (of amplitude larger than 20° in Chow & Adams (2011)) associated with a periodic lateral deviation of the centre of gravity, about the cylinder configuration corresponding to the rectilinear path with the symmetry axis perpendicular to the mean fall velocity. Numerical simulations by Romero-Gomez & Richmond (2016) reproduced the results of Chow & Adams (2011). Jayaweera & Mason (1965) investigated small cylinders made either of Perspex, steel or aluminium falling in liquid paraffin, sugar solutions of different concentrations or water, for Reynolds numbers ranging from less than 0.01 to approximately 1000. They observed that when eddies break away from the edges as well as the sides, the cylinder flutters with an amplitude of oscillation comparatively larger for shorter cylinders, but decreasing as the length increases, so that longer cylinders fall stably. They further mentioned that the transition from steady fall to fluttering is not abrupt. They however observed that it depends on $\overline{\rho}$, and that the critical value of Re above which fluttering occurs increases with increasing L/d; for steel cylinders with L/d about 10, their critical value of Re is approximately 50. Marchildon *et al.* (1964) observed the secondary motion for Re greater than 300, and in some cases as low as 80. It is worth pointing out that the latter value is higher than the critical Reynolds number corresponding to the onset of unsteadiness in the wake behind a fixed two-dimensional cylinder of infinite span, $Re_c \simeq 47$. However, for a cylinder held in an upcoming flow, the transition of its wake from a stationary to a periodic state is strongly dependent on the elongation ratio L/d of the cylinder. The experiments by Schouveiler & Provansal (2001) and Provansal, Schouveiler & Leweke (2004) for cylinders with free hemispherical ends and the numerical simulations by Inoue & Sakuragi (2008) for cylinders with free flat faces indicate that this transition occurs at increasing critical Reynolds numbers Re_c when the elongation ratio decreases, typically $Re_c \simeq 100$ for $L/d = 5$ and $Re_c \simeq 200$ for $L/d = 1$. Furthermore, the numerical investigation by Inoue & Sakuragi (2008) disclose the existence of a variety of wake structures for $40 \leqslant Re \leqslant 300$ and $1 < L/d < 100$. Depending on the governing parameters, they identify five different vortex shedding patterns, corresponding to different equilibria reached from the vortical contributions generated from the flat bases or from the circular side of the cylinder. A question thus arises regarding what would be the paths associated with these different wake structures, or how would these be modified by the degrees of freedom of the cylinder.

Besides the diversity of paths that could be observed, we have seen that the question of the existence of contrasted periodic motions of either low or large amplitude associated with different types of wake structure, permeates the literature on freely moving two-dimensional cylinders. As this feature is shared with disks, or spheres, conviction has grown steadily stronger that it constitutes a central question concerning the behaviour of freely moving bodies (Ern *et al.* 2012). A decisive step forward to clarifying this question was achieved recently for short-length cylinders (‘disks’ of variable thickness), by a joint effort in both direct numerical simulations (Auguste, Magnaudet & Fabre 2013; Chrust, Bouchet & Dušek 2013) and stability analysis

of the fluid–body system (Tchoufag, Fabre & Magnaudet 2014). Tchoufag *et al.* (2014) showed that instability of the fluid–body system leads to contrasted instability modes corresponding to different strengths of coupling between the body and the fluid depending on the time scales involved, resulting in different types of paths, in particular periodic motions of contrasted amplitude, but also involving different symmetry properties, embodied in planar or spiralling paths, or intermediate paths. The existence of modes corresponding to different strengths of coupling between the fluid and the body may also be expected to occur for finite-length elongated cylinders. Furthermore, these complex regimes are more likely to happen close to the onset of path instability where the rectilinear path gives way to periodic paths.

With the aim of shedding some light on the questions raised in this introduction, the present paper addresses experimentally the problem of freely falling finite-length cylinders for a large range of elongation ratios and Archimedes numbers corresponding to paths transitioning from rectilinear to periodic. The general guideline of this work is the following. We first present the experimental approach, in particular the experimental set-up allowing us to track the motion of the cylinders, and the image processing procedure implemented to have a non-biased and accurate description of it. A technical appendix complements the latter. We then present an overview of the different paths observed. The following sections are devoted to the quantitative characterization of the rectilinear and fluttering paths, presenting the measurement results and the corresponding scaling laws for the mean vertical motion as well as for the oscillatory translational and rotational motion of the body. A qualitative description is further provided, when possible, of the wake structure associated with the different paths. The paper ends with a discussion and concluding remarks.

2. Experimental tools

The bodies used in the experiments are '3D printed' elongated circular cylinders of length L and diameter d. The 3D printer was a ProJet®3510HD, and the material, VisiJet®M3-X, an ABS-like plastic. The choice of 3D printing allowed us for a very good control of the dimensions of the cylinders, with a resolution of 32 μm and an accuracy of $\pm 2‰$. When possible, cylinders were printed with their axis pointing upwards, so that the layers of material were deposited along the length of the cylinder, which allowed for a better accuracy when printing the rounded sides of the cylinder. However, this could not be done for very long cylinders ($L/d = 20$), for they would bend during the printing process. Consequently, the latter were printed with their axis horizontal. The diameter of the cylinders ranged from 1.17 to 5.47 mm, and their lengths from 5.26 to 50.86 mm. The elongation ratio of the cylinders L/d ranged from 2 to 20 and was known to within $\pm 4.3 \times 10^{-2}$. The mass of all cylinders was measured using a scale accurate up to 10^{-4} g, which allowed us to know the density ρ_c of the cylinders with an accuracy of ± 0.2 kg m^{-3}. The measured densities ranged from 1140.0 to 1190.0 kg m^{-3}, with two cylinders out of 163 having a measured density of 1111.0 kg m^{-3}. The cylinders were kept submerged in water at all times to ensure that the porosity of the 3D printing material was constantly saturated with water, so that the body density would not change during the course of the experiments. At the minimum three different cylinders were printed for each couple of parameters (L, d). No significant difference in behaviour was observed across all bodies having same dimensions (L, d), which ensures that the 3D printing was consistent both with dimensions and density of the bodies.

The experiments were performed in a 1.70 m high glass tank with a square cross-section of 0.4 m (eight to eighty times larger than the particle length), filled with

filtered tap water. The tank was located in an air-conditioned laboratory at $19 \pm 1\,^{\circ}\mathrm{C}$. Water temperature was measured everyday using two thermocouples located at the top of the tank below the free surface, and at the bottom of the tank. Temperature differences between the top and the bottom of the tank were always smaller than $1.1\,^{\circ}\mathrm{C}$. The water density was assumed to be $\rho_f = 1000$ kg m^{-3}, giving a density ratio of $\overline{\rho} = \rho_c/\rho_f = 1.16 \pm 1\,\%$ for all experiments.

In addition to the density ratio $\overline{\rho}$ and the elongation ratio L/d, the problem also depends on the Archimedes number, introduced previously and defined as,

$$Ar = \left(\frac{\rho_c - \rho_f}{\rho_f} g D\right)^{1/2} \frac{D}{\nu} \quad \text{with } D = \left(\frac{3}{2} d^2 L\right)^{1/3}, \tag{2.1}$$

where the diameter of the sphere having a volume equal to that of the cylinder is taken here as the characteristic dimension of the body D. With this definition of Ar based on D, experiments performed for various L/d at given Ar and $\overline{\rho}$ allow us to investigate for given volume, and thus given buoyancy force, the influence of the cylinder elongation ratio on its behaviour.

The cylinders were released at the top of the tank, below the free surface, using tweezers. The release conditions were found to have no effect on the final behaviour of the cylinder. Even when released with their axis vertical, the cylinders rotated so that their axis was horizontal after a transient distance of fall less than $10d$. The time between two releases was kept above 5 min, so that fluid perturbations in the tank caused by the fall of the previous cylinder could dissipate.

The cylinders were tracked along their fall with a travelling cart embarking two orthogonal cameras and the corresponding backlights allowing the observation of the bodies by shadowgraphy (figure 1*a*,*b*). Travelling followed the cylinders over a distance of at least $200d$. The elevation of the cart was recorded using a magnetic encoder with an accuracy of ± 5 μm and an acquisition frequency of 1000 Hz. Since the shadowgraphy technique could not provide any information on the cylinder rotation about its axis, a pattern of random dots was drawn on a single cylinder out of the three available for each set of parameters $(Ar, L/d, \overline{\rho})$. Use of front lightning allowed visualization of these patterns. No significant rotation of the cylinders about their axes was observed across all experiments, except in some cases during the short transient period following the release of the body from rest.

In addition, specific experiments were carried out to uncover the wake associated with the different types of path. The wake of the falling cylinders was visualized by coating the bodies with ink before releasing them in the tank. The ink chosen was highly concentrated and miscible in water. The cylinders were left submerged in pure ink during 15 to 30 min before being released in the tank, to ensure that the amount of ink on the cylinder surface was sufficiently high so that it would be released during a satisfactory amount of time. The ink trail left by the cylinders during their fall was recorded with the same cameras and backlights used for shadowgraphy.

3. Image and signal processing

The images were acquired by two orthogonal cameras using shadowgraphy, i.e. by shedding light from behind the cylinder, which projects its shadow on the camera (figure 1*b*). The output of the cameras is two grey scale image sequences in the planes (X, Z) and (Y, Z), where Z is the vertical coordinate and (X, Y) map the horizontal plane. Two different sets of cameras were used. PCO2000® acquired 2048×2048

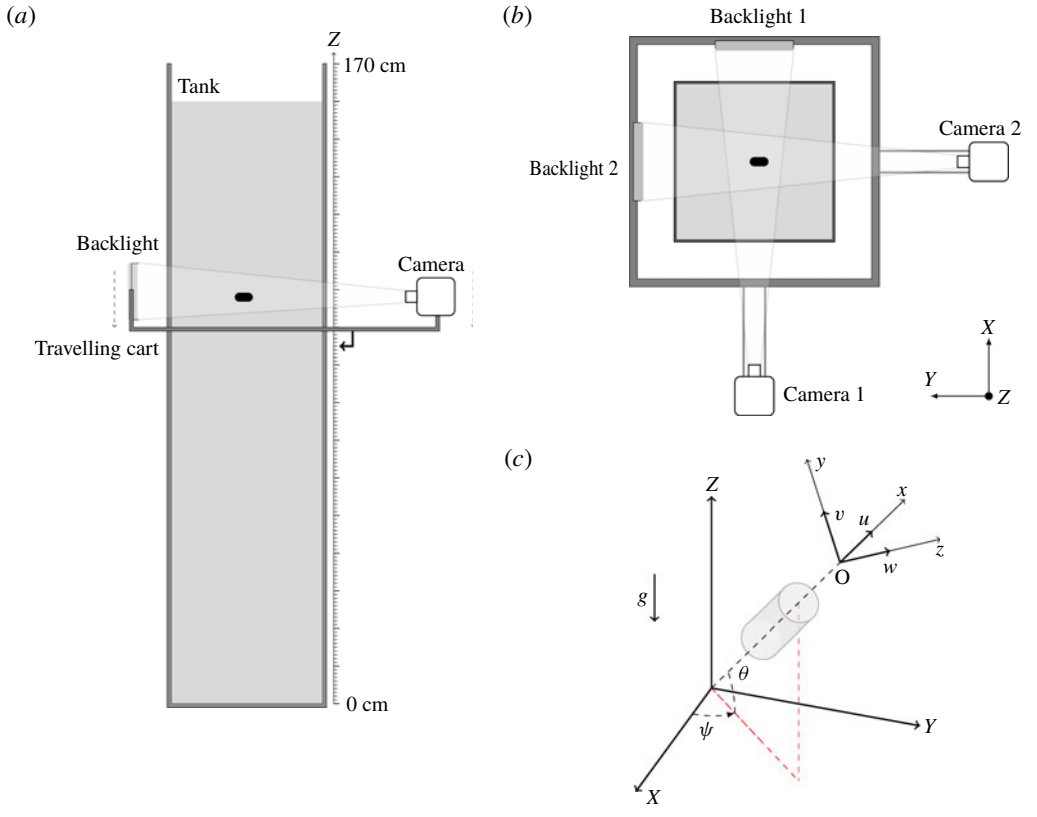

FIGURE 1. (Colour online) (*a–b*) Lateral and top view of the experimental set-up; (*c*) schematic view of the cylinder; (*b–c*) definition of the coordinate systems. Z labels the vertical coordinate, (X, Y) the horizontal plane defined by the positions of the cameras. Origin O is fixed; axis (Ox) is parallel to the cylinder axis; (Oz) is parallel to the horizontal plane (X, Y); plane (x, y) is vertical.

pixels images at 14 Hz for recording slow periodic motions, and LaVision® sCMOS acquired 2560×2160 pixels images at 50 Hz for faster oscillations. The grey scale images were converted to black and white images using a thresholding operation. After binarization, the cylinder shadows on both cameras appear as a black area on a white background. The list of pixels belonging to the borders between black and white regions was then retrieved and labelled as the projection contours of the cylinder. Following the routine described in Fernandes *et al.* (2007), camera calibration was performed using a metallic cylinder of known diameter, which was placed at different known positions (X_{cal}, Y_{cal}) in the cameras field of view. The optical scale factor obtained with the camera calibration was used to convert the pixel data of the images in metres. Then, an iterative procedure crossing the information provided by the two cameras allowed the estimation of the three-dimensional (3-D) coordinates of the cylinder centre of gravity as those of the isobarycentres of the contour points of the cylinder projections. This method is however not sufficient to determine accurately the centre of gravity and orientation of the body, as it does not account for the deformations of the cylinder contour induced by the perspective projections onto the image plane of the cameras. It provides however a first estimation of the distance

of the body centre to the camera which is used as an initialization of the refined following step implemented to correct perspective effects. This advanced technique, described in more details in the Appendix, is based on a geometric reprojection of the cylinder contour (Huang, Chen & Chia 1996). It outputs the centre of the two flat faces of the cylinder, denoted S and T, in a frame tied to the camera position. Using the vertical position of the travelling cart embarking the cameras, given by the magnetic encoder, the positions of S and T can then be expressed in a frame tied to the tank (thereafter termed the laboratory frame), which is independent of the position of the travelling cart, and corresponding to the coordinate system (X, Y, Z).

From the 3-D coordinates of S and T, the position of the cylinder centre of gravity can easily be deduced, as well as the angle θ between the cylinder axis and the horizontal, and the azimuthal angle ψ (see figure 1*c*). Note that, as mentioned in § 2, experiments showed that no rotation of the cylinder about its symmetry axis could be observed, apart from the initial transient in some cases. However, transients, mainly related to the release of the body from rest, are discarded in the analysis and results that follow. The 3-D coordinates of the cylinder centre of gravity in the laboratory frame are hereafter denoted (X, Y, Z), and the corresponding velocities (u_X, u_Y, u_Z). An example of the time evolution of the quantities characterizing the cylinder position and orientation can be seen in figure 2(*a–d*). In addition to the oscillatory behaviour, a slight drift is observed for the spatial coordinates X and Y, as well as for the azimuthal angle ψ. This drift was measured to be always less than 6 % of the total falling height, to be not reproducible and could not be linked to any of the governing parameters. Its existence is attributed to large-scale low-velocity fluid motions in the tank, as they are difficult to avoid in a large tank. Similar irregular weak motions were observed in other experiments, and are mentioned in particular by Fernandes *et al.* (2007) for the study of rising disks. Following their approach that considers this drift as uncoupled with the main oscillatory motion of the body, a low-frequency filtering is applied to the time evolutions of the quantities characterizing the oscillatory behaviour of the body. The amplitude and phases of the periodic signals are then obtained using the Hilbert transform.

The coordinate system provided by the cameras being arbitrary, it is not the best suited to describe the body motion. Several coordinates systems can be introduced to get a better characterization of the body motion. For planar trajectories of the cylinders, a simpler and good description of their path is in fact manifest in the azimuthal plane defined by the cylinder axis and the vertical direction, and obtained by rotating the laboratory frame coordinates (X, Y, Z) by the angle ψ, as

$$\begin{bmatrix} X_{azi} \\ Y_{azi} \\ Z_{azi} \end{bmatrix} = R_\psi \begin{bmatrix} X \\ Y \\ Z \end{bmatrix} \quad \text{with } R_\psi = \begin{pmatrix} \cos\psi & \sin\psi & 0 \\ -\sin\psi & \cos\psi & 0 \\ 0 & 0 & 1 \end{pmatrix}. \tag{3.1}$$

However, while it is often the case, we will see later that not all trajectories lie in this plane. We therefore opt to work within the frame, hereafter termed the body frame, having its origin O fixed and axes (x, y, z) rotating with the body (Lamb 1993). Axis (Ox) is chosen parallel to the cylinder axis and the plane (x, y) vertical (see figure 1*c*). In this frame, the cylinder velocity components are denoted (u, v, w) and are deduced from the velocity components in the laboratory frame (u_X, u_Y, u_Z) by two rotations of angle θ and ψ respectively,

$$\begin{bmatrix} u \\ v \\ w \end{bmatrix} = R_\theta R_\psi \begin{bmatrix} u_X \\ u_Y \\ u_Z \end{bmatrix} \quad \text{with } R_\theta = \begin{pmatrix} \cos\theta & 0 & \sin\theta \\ 0 & 1 & 0 \\ -\sin\theta & 0 & \cos\theta \end{pmatrix}. \tag{3.2}$$

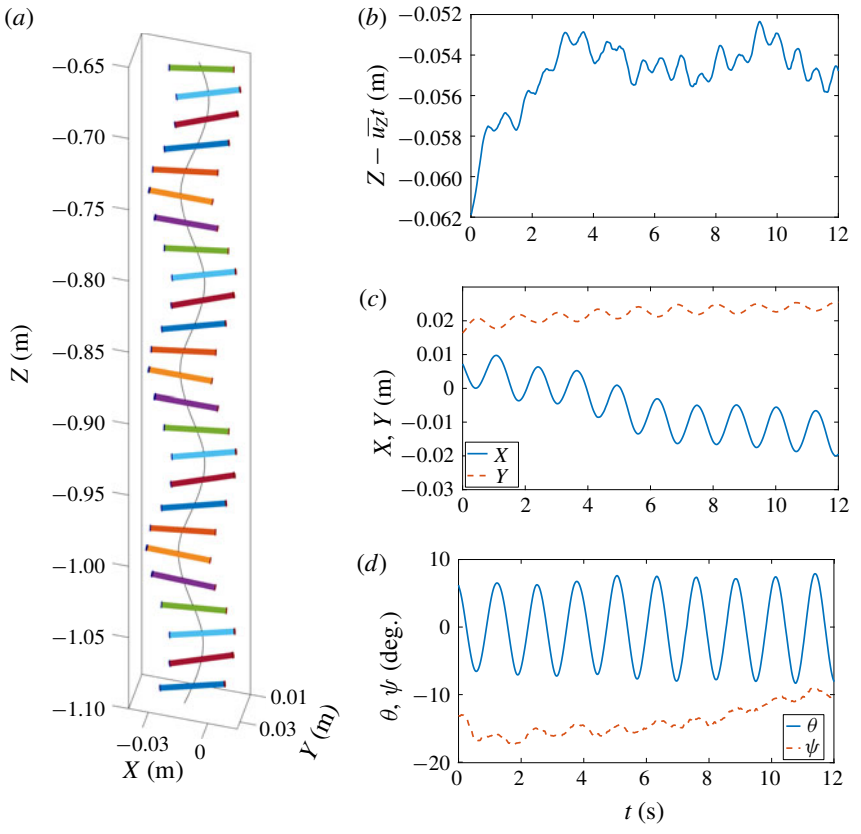

FIGURE 2. (Colour online) Illustration of the cylinder motion in the fluttering regime: (*a*) three-dimensional plot, with an angle of view chosen close to perpendicular to the azimuthal plane to avoid perspective effects; corresponding time period 5.5 s to 10.5 s; the cylinder is plotted every 0.18 s. (*b–d*) Typical evolutions in time of the: (*b*) vertical displacement, (*c*) horizontal coordinates, (*d*) angles θ and ψ; $Ar = 800$, $L/d = 10$, $d =$ 3 mm, $\overline{u_Z} = 10$ cm s^{-1}.

Note that the axis z, corresponding to the velocity component w, has been chosen perpendicular to the vertical plane (x, y), and is therefore horizontal. As can be seen in the example in figure 3, the body frame provides a simpler and more relevant description of the body motion than the laboratory frame, figure 3(*b*) indicating that in this case, the trajectory is nearly planar and contained in the azimuthal plane.

4. Overview of the different paths observed

In this section we provide an overview of the different types of path observed within the space of parameters $(Ar, L/d)$ investigated for 195 cylinders. As can be seen in figure 4, three main types of motion are observed in the range $Ar \in [200, 1100]$, $L/d \in [2, 20]$. The first two correspond to stationary regimes: the rectilinear fall and the regular oscillatory motion called fluttering. In addition, in the transitional region of parameters separating the domains of occurrence of these regimes, oscillatory motions of weak and irregular amplitude are detected. Based on their distinctive features, we separate them in three types (termed Irregular I to III).

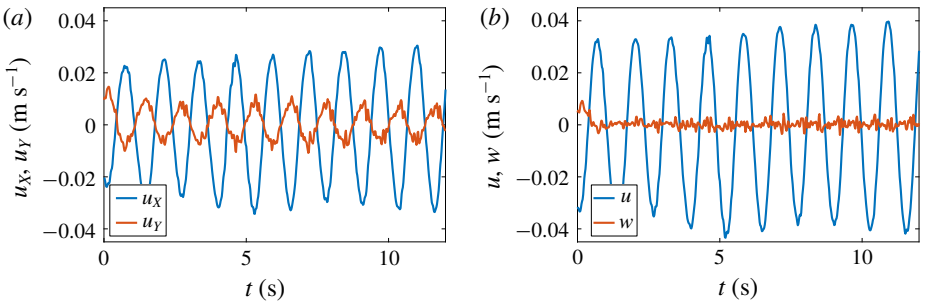

FIGURE 3. (Colour online) Comparison of the velocity components (a) in the laboratory frame, and (b) in the system of axes rotating with the body defined in figure 1(c); $Ar = 800$, $L/d = 10$.

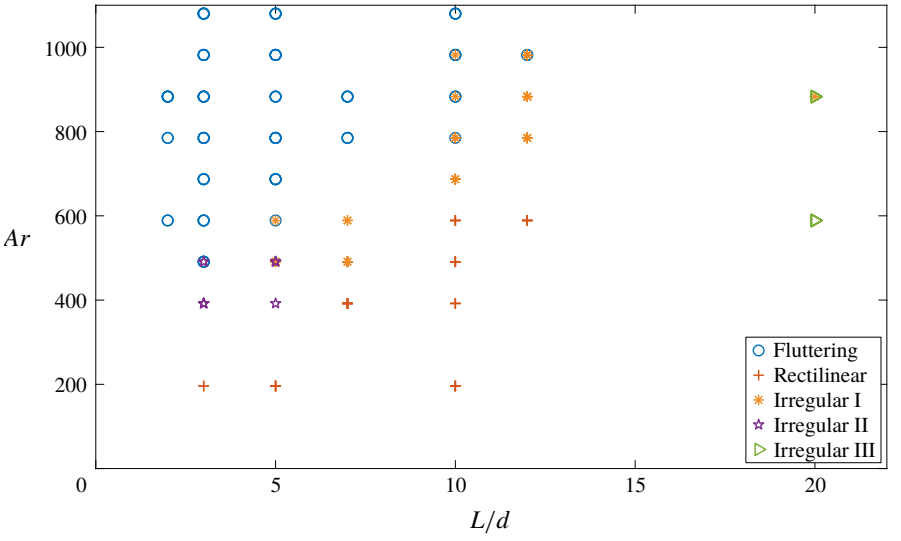

FIGURE 4. (Colour online) Map of the different paths observed in the plane $(Ar, L/d)$ for $\rho_c/\rho_f \simeq 1.16$. For all $(Ar, L/d)$, each type of path is observed using different cylinders. For some $(Ar, L/d)$, different types of path can be observed with the same cylinder in different runs.

The fluttering motion is a periodic oscillatory motion of regular amplitude, observed here for Archimedes numbers ranging from 490 to 1080, and L/d from 2 to 12 (figure 4). An illustration of this path is shown in figure 2(b–d), where the evolution in time of the five measured degrees of freedom are plotted. The evolution of the body along its path is also displayed in the three-dimensional plot of figure 2(a). Fluttering typically occurs for heavier and shorter cylinders, at a frequency of approximately 1 Hz. It is characterized by oscillations of the cylinder centre of gravity (horizontal displacement in the azimuthal direction ranging approximately from $0.1L$ to $0.3L$, or $0.35d$ to $2.8d$) coupled with oscillations of the inclination angle θ (ranging from 7° to 20°). Oscillations of horizontal velocity components (u_X, u_Y) and of θ occur at the same frequency f and their amplitudes remain constant during the fall. Owing to symmetry properties, oscillations of the vertical velocity component u_Z occur at twice

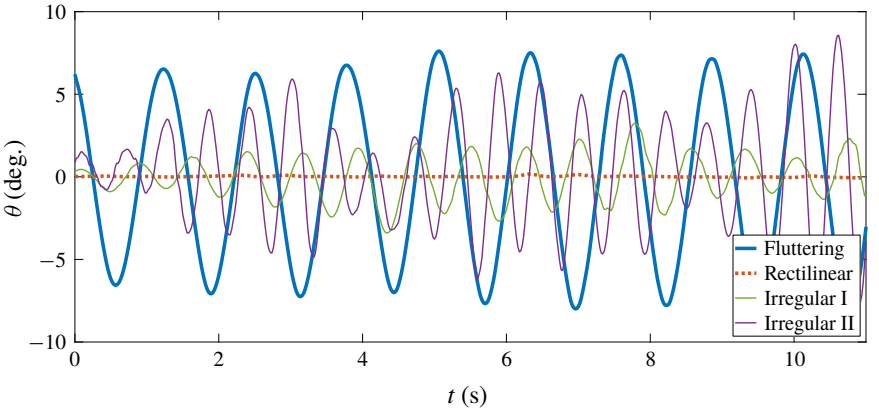

FIGURE 5. (Colour online) Examples of the time evolution of θ for the fluttering motion ($Ar = 785$, $L/d = 10$), for the rectilinear motion ($Ar = 200$, $L/d = 3$), for the Irregular I motion ($Ar = 500$, $L/d = 5$) and for the Irregular II motion ($Ar = 400$, $L/d = 3$).

the fluttering frequency, $2f$. Weak oscillations of ψ (typically lower than 6°) can also be observed at the fluttering frequency, and are stronger for cylinders with smaller elongation ratios ($L/d < 5$). The kinematics of the fluttering regime will be described in detail in § 6. Similar zigzag periodic motions were observed for finite-length cylinders covering a large range of density ratios (see for instance Marchildon *et al.* 1964; Chow & Adams 2011), and are also known to exist for plates (see for instance Belmonte, Eisenberg & Moses 1998; Andersen, Pesavento & Wang 2005*b*) and disks (see for instance Fernandes *et al.* 2007; Auguste *et al.* 2013).

During the rectilinear vertical fall, the cylinder axis remains horizontal. This kind of motion is observed in a subspace of $Ar \in [200, 1000]$ and $L/d \in [3, 12]$ (figure 4). For this type of path, a slight horizontal drift might be observed on the motion of the centre of gravity, but it is weak (for all cases it is lower than 3 % of the total falling height), non-reproducible and does not present a preferential direction related to the body geometry. No significant and regular horizontal motion could be observed for these cylinders so that their path is termed rectilinear. However, low-amplitude high-frequency oscillations (approximately six times larger than typical fluttering frequencies f) were detected on the vertical velocity u_Z (or on v) in the range $L/d \in [2, 12]$ and $Ar \in [390, 1080]$ investigated with a 50 Hz acquisition frequency of the camera, and covering both some rectilinear and fluttering paths. These oscillations will be discussed in more detail in § 7.

In the transitional region separating the rectilinear fall and the fluttering regime, different types of weak irregular oscillations can be observed, markedly in contrast with the rectilinear and fluttering regime. Though they are hard to disentangle from noise, some distinctive features can be pointed out to suggest a classification. The regime Irregular I is attributed to cylinder oscillations of weak and irregular amplitude in both displacement and inclination angle θ. These occur at frequencies close to those of the fluttering motion but with amplitudes significantly smaller (typically $\theta < 3°$) and less regular than the ones observed for fluttering cylinders. An illustration is provided in figure 5. In the regime Irregular II observed here for $Ar \in [400, 500]$ and $L/d \in [3, 5]$, the oscillations of the cylinder axis (close to the fluttering frequency f) are modulated by a low-frequency oscillation (for instance, six times slower), as

shown in figure 5. The amplitude reached in the bursts is higher than that observed in the regime Irregular I (for instance, an amplitude of 10° can be reached). As for now, the origin of this mode is unclear, but it might be related to a complex wake structure occurring for this range of parameters. In fact, it is worth pointing out that low-frequency modulations of wake oscillations have been observed in several studies for fixed finite-length cylinders with free ends in comparable ranges of L/d and Re. Dauchy, Dušek & Fraunié (1997) observed a slow modulation of the oscillations in the wake of cylinders with L/d about 10 and 20 for $52 \leqslant Re \leqslant 100$, as the result of a secondary instability setting in at approximately 20 % above the primary instability threshold. Numerical simulations by Inoue & Sakuragi (2008) for cylinders with $20 \leqslant L/d \leqslant 50$ and $Re = 60$ also revealed the existence of a low-frequency modulation in the wake signal, but the beat in this case was attributed to bistability of the flow and the alternate appearance of two different modes of instability (namely Type II and III described here in § 7). Note that the frequency of the wake primary instability is different in both studies, both values being approximately seven times larger than the frequency f of the modulated oscillation observed here. Regimes Irregular I and II are difficult to distinguish from what would be the fluttering regime when it sets in. And in fact, figure 4 shows that for different cylinders having same (Ar, L/d), different types of path (fluttering, Irregular I or II) can be observed. This underlines the difficulty of experimentation for these parameters. However, as will be seen later in figure 12, there is a significant jump in the oscillation amplitude of θ between the regime Irregular I and the fluttering one. Finally, in the case of long cylinders ($L/d = 20$, $Ar = 590$ and $Ar = 890$), a different rotational low-amplitude oscillatory mode is observed, called Irregular III. At variance with the fluttering mode that affects the inclination angle θ, regime Irregular III is characterized by oscillations in the azimuthal angle of the cylinder, ψ, occurring at a higher frequency than the fluttering one, approximately 4 Hz. The amplitude of this motion is of extremely low amplitude, approximately 0.2°.

We have seen that a wide variety of paths occurs for cylinders in the range of parameters investigated here. The existence of low-amplitude oscillatory motions and the subsequent transition to stronger oscillations, when control parameters are changed (in this case for given L/d when increasing the volume of the body, i.e. when increasing Ar) has been observed in previous works for bodies with contrasted geometries (disks, short-length cylinders, two-dimensional cylinders, spheres, etc ...) as reviewed by Ern *et al.* (2012). As the experimental determination of these motions, termed A-regimes or quasi-vertical regimes in the literature, may be hindered or modified by noise or residual disturbances in the fluid, numerical simulations appear today as the most suitable tool for their investigation (Auguste *et al.* 2013; Chrust *et al.* 2013). We therefore turn now our attention to the quantitative analysis of mean fall velocity and mean drag (§ 5), before focusing on the properties of the large-amplitude oscillatory motion corresponding to the fluttering regime (§ 6).

5. Mean fall velocity of the cylinder

After the initial transient following the release of the body from rest, a mean vertical velocity of the body can be determined. Its absolute value, denoted $\overline{u_Z}$, typically ranges from 4 to 13.5 cm s^{-1}. For a given couple ($Ar, L/d$), data scattering between different runs indicates on average a relative error for $\overline{u_Z}$ less than 1 % for the whole data, with a maximum of dispersion of 4.5 %. The velocity $\overline{u_Z}$ can be used to create the Reynolds number $Re_d = \overline{u_Z} d/\nu$ based on the cylinder diameter, which is particularly

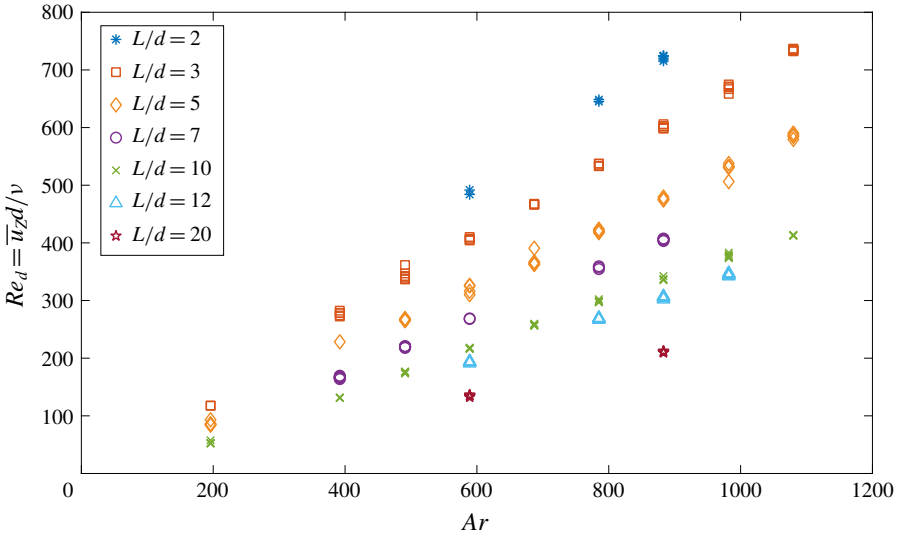

FIGURE 6. (Colour online) Reynolds number versus Archimedes number for various elongation ratios.

useful for the comparison with fixed or with two-dimensional cylinders, as will be done in § 7. Figure 6 shows Re_d plotted versus the Archimedes number for various L/d. For a given volume of the body, corresponding to a given Archimedes number, a strong effect of the elongation ratio is visible, lower L/d corresponding to higher Re_d. For all elongation ratios and all types of motion, the evolution of Re_d versus Ar is very close to linear, though for $L/d \leqslant 5$ and $Ar \leqslant 500$, data more notably separate from the global trend.

A drag coefficient can also be deduced from $\overline{u_Z}$, via a force balance between the drag force and the buoyancy force, as

$$\frac{1}{2}\rho_f C_d L d \overline{u_Z}^2 = (\rho_c - \rho_f)\frac{\pi}{4} d^2 L g, \tag{5.1}$$

$$\text{giving } C_d = \frac{\pi}{2}\frac{\rho_c - \rho_f}{\rho_f}\frac{gd}{\overline{u_Z}^2}. \tag{5.2}$$

Figure 7 shows the evolution of C_d with the Reynolds number for the different types of motion. The drag coefficients are nearly constant at 0.70 for the fluttering and Irregular I regime, for the Reynolds numbers and elongation ratios considered here, and for rectilinear paths with $Re_d > 250$. Irregular II paths also correspond to comparable values of C_d. For rectilinear paths with Re increasing from 50 to 250, the drag coefficient decreases from about 1.45 to 0.70. Cylinders undergoing Irregular III oscillations have a higher C_d than those falling rectilinearly at the same Re_d, an increase of approximately 0.1 being observed for $Re_d \simeq 100$ and of 0.15 for $Re_d \simeq 200$. For comparison, we also plot the drag coefficients obtained experimentally by Jayaweera & Mason (1965) for metal cylinders with $L/d > 100$ falling through liquid paraffin, sugar solutions or water. The trend is similar, but the two sets of measurements separate on parallel curves for $Re_d > 50$, a difference that may come from the differences in $\overline{\rho}$ and L/d. For $10 < Re_d < 50$, we also compare with the

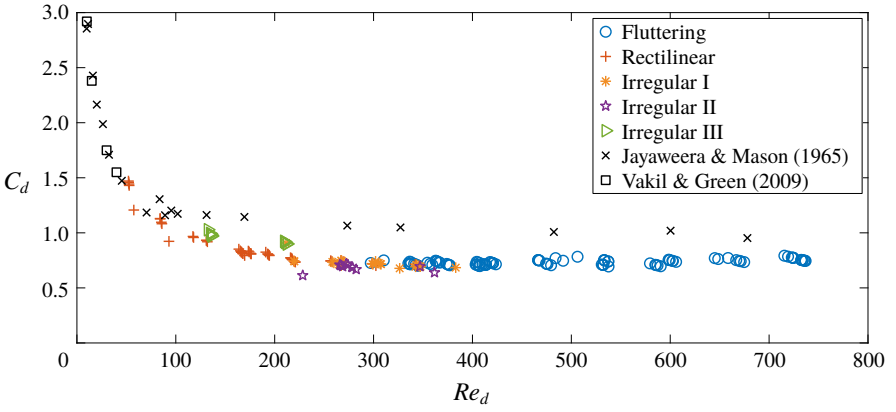

FIGURE 7. (Colour online) Drag coefficient of the freely falling cylinders versus Reynolds number $Re_d = \overline{u_Z} d/\nu$ for the different types of motion, and comparison with some previous works.

coefficients provided by the numerical simulations of Vakil & Green (2009) for fixed finite-length cylinders. Their results are consistent with those of Jayaweera & Mason (1965) and with the trend of our data. In this range of Re, no significant effect of L/d is observed by Vakil & Green (2009). In their experimental study on the drag coefficient of freely falling cylinders for $200 < Re_d < 6000$, Chow & Adams (2011) review the different correlations of the literature based on $\overline{\rho}$ and L/d, and propose an expression depending on $I^* = \sqrt{\overline{\rho}/(L/d)}$. In the present study, the drag coefficient depends on the Reynolds number for $Re_d < 200$, which lies outside the range of Re_d studied by Chow & Adams (2011). However, significant differences in C_d are also observed with this work for $Re_d > 200$ for the same values of $\overline{\rho} = \rho_c/\rho_f$ and L/d. Chow & Adams (2011) measured C_d ranging from approximately 0.8 to 1 for I^* ranging from 0.25 to 1, whereas the present C_d is nearly constant at 0.7 over the same range of I^*. This difference might be linked with the fact that the fluttering motion observed by Chow & Adams (2011) is of a much greater amplitude ($20° < \tilde{\theta} < 50°$) than the one observed in the present study, where $\tilde{\theta} < 25°$.

The remarkable trend displayed by the evolution of C_d with Re_d in figure 7 allows us to infer from equation (5.2) that the characteristic velocity scale for the mean fall is given by the gravitational velocity $u_0 = ((\rho_c/\rho_f - 1)gd)^{1/2}$. The dimensionless mean fall velocity $\overline{u_Z}/u_0$ is shown in figure 8 for all the Archimedes numbers and elongation ratios investigated. For fluttering and Irregular I regimes, as well as rectilinear paths with $Ar > 600$, the dimensionless velocity is remarkably independent of the Archimedes number; $\overline{u_Z}/u_0$ is almost constant at approximately 1.46 for all the Ar and L/d considered here. In the case of cylinders falling rectilinearly with Archimedes numbers rising from approximately 200 to 600, the fall velocity increases from approximately 1 to 1.5 and depends on the elongation ratio, as can be seen in the inset of figure 8. The effect is stronger at lower Ar. For $Ar = 200$, a difference of about 0.2 is observed between $L/d = 10$ and $L/d = 3$, longer cylinders being the slower ones. A slight effect of the type of motion is also visible. Cylinders undergoing modulated oscillations (regime Irregular II) have a slightly higher dimensionless fall velocity than those displaying fluttering and rectilinear paths (difference of approximately 10 % for $Ar = 400$ and 5 % for $Ar = 500$), while cylinders undergoing weak azimuthal

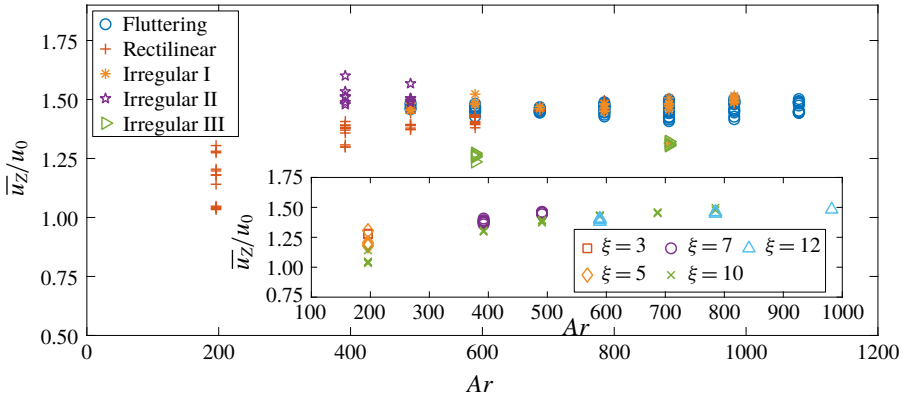

FIGURE 8. (Colour online) Average vertical velocity scaled by the gravitational velocity versus the Archimedes number for the different types of motion. The inset shows the effect of the elongation ratio on the velocities of cylinders displaying a rectilinear motion.

oscillations (regime Irregular III) have a lower (approximately 20 %) dimensionless fall velocity than the other ones. Interestingly, for bodies undergoing a fluttering motion, the mean fall velocity of the elongated finite-length cylinders considered here scales with the gravitational velocity u_0 based on their diameter d independently of their length L, in the same way the mean fall/rise velocity of short-length cylinders (disks of finite thickness) scales with the gravitational velocity based on their length or thickness L, independently of the body diameter (Fernandes *et al.* 2007).

6. Fluttering regime of the cylinders

This section focuses on the study of the body kinematics in the oscillatory regime, called fluttering in § 4, and characterized by oscillations of the body centre of gravity and of the body inclination, θ. These oscillations occur at the frequency f with $\omega = 2\pi f$, while oscillations at 2ω are observed on the vertical velocity of the body. The fluttering frequency f was measured via a spectral analysis of the oscillations of θ over the time span corresponding to a constant amplitude. The frequency ranges from 0.65 to 1.5 Hz and decreases as Ar increases, whatever the elongation ratio. For $L/d = 2$, a frequency decrease from approximately 1.5 to 1.2 Hz is observed for Ar going from approximately 590 to 880. For $L/d = 10$, f goes from 0.80 to 0.75 Hz for Ar increasing from 785 to 1090. To build a Strouhal number, a characteristic length scale has to be chosen as a complement to the gravitational velocity determined in the previous section, u_0. Considering the classical interpretation of the Archimedes number as a Reynolds number, we note that $Ar = \sqrt{3/2}u_0 l_0/\nu$, with $l_0 = \sqrt{dL}$. The characteristic length and velocity scales, l_0 and u_0, can then be used to form the Strouhal number,

$$St^* = fl_0/u_0 = f\sqrt{dL}/u_0. \tag{6.1}$$

Figure 9 shows that St^* is nearly independent of Ar and L/d in the range considered, with $St^* \simeq 0.11$. Furthermore, this result turns out to be general for short and elongated finite-length cylinders. For short-length cylinders with L/d ranging from 0.1 to 0.5 and a density contrast close to 1, Fernandes *et al.* (2007) obtained the relation $St^* = fd/((\rho_c/\rho_f - 1)gd)^{1/2} \simeq 0.1$ which is retrieved from the expression (6.1) proposed

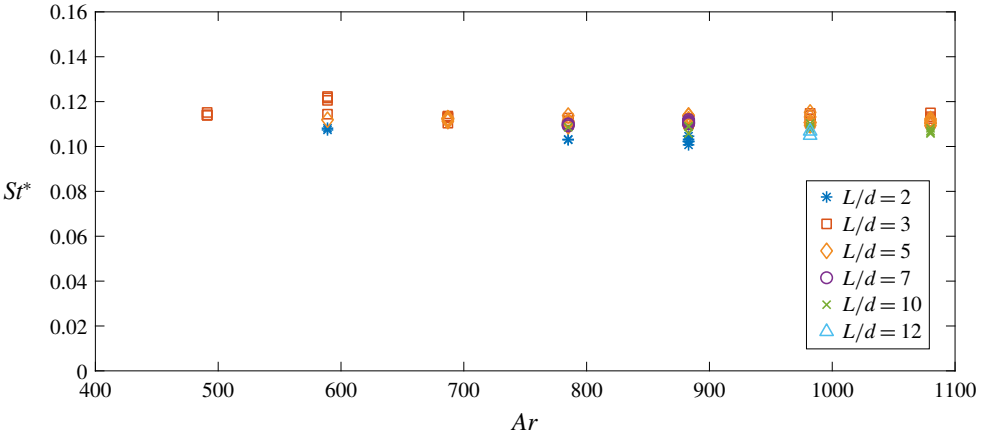

FIGURE 9. (Colour online) Strouhal number $St^* = f\sqrt{Ld}/u_0$ of the fluttering motion versus the Archimedes number Ar for various elongation ratios.

here, considering that the gravitational velocity scale u_0 for these bodies is $((\rho_c/\rho_f - 1)gL)^{1/2}$, L being the cylinder length or disk thickness. It is worth pointing out that the Strouhal number St_L based on the inertial time scale L/u_0 is also nearly independent of Ar for all L/d but contrastingly shows a strong dependence in L/d, increasing from approximately 0.15 for $L/d = 2$ to approximately 0.4 for $L/d = 12$. In fact, St_L scales with $(L/d)^{1/2}$, so that $St_L/(L/d)^{1/2} \simeq 0.11$ for all elongation ratios and Ar considered here. A similar expression can be straightforwardly obtained for the Strouhal number based on the diameter d.

This result can be compared with the expression $f_{lit} \simeq 0.126\sqrt{(\overline{\rho} - 1)g/\overline{\rho}L}$ proposed by Marchildon *et al.* (1964) to represent the oscillation frequencies they measured experimentally for cylinders with $\overline{\rho} \in [1.14, 11.7]$ and by Chow & Adams (2011) for cylinders with $\overline{\rho} \in [1.13, 8.51]$. This expression fits, with only a very slight overestimation, the measured oscillation frequencies f of the present paper, since $f_{lit} \simeq 1.14f/\sqrt{\overline{\rho}} \simeq 1.06f$ for $\overline{\rho} = 1.16$. However, the two predictions significantly depart from each other for stronger density contrast $\overline{\rho}$. A factor 2 between the two expressions would typically be found for metal cylinders falling in water. It is therefore worth pointing out that both expressions have to be considered with caution. The expression proposed here, which also applies to short-length cylinders, was only determined for bodies with a density close to that of the surrounding liquid. As in the case of short-length cylinders (or disks), at different $\overline{\rho}$, different modes of oscillatory motion may be expected to occur (Tchoufag *et al.* 2014). As regards the expression for f_{lit}, it is based on a torque balance on the body, assuming that the moment of momentum of the cylinder compensates for a pressure torque due to the asymmetry of the flow surrounding the cylinder, as soon as its axis is no longer perpendicular to its velocity. However, this balance omits the added-mass torque related to the existence of both axial and transversal velocity components, and which has been lately shown to provide a crucial contribution for anisotropic bodies, for instance for plates (Andersen, Pesavento & Wang 2005*a*) and short-length cylinders (Fernandes *et al.* 2008). Like for these bodies, the selection of the fluttering frequency is therefore concealed in the intricate equilibrium between the proper and added inertia terms and the vortical contributions accounting for viscous and wake effects.

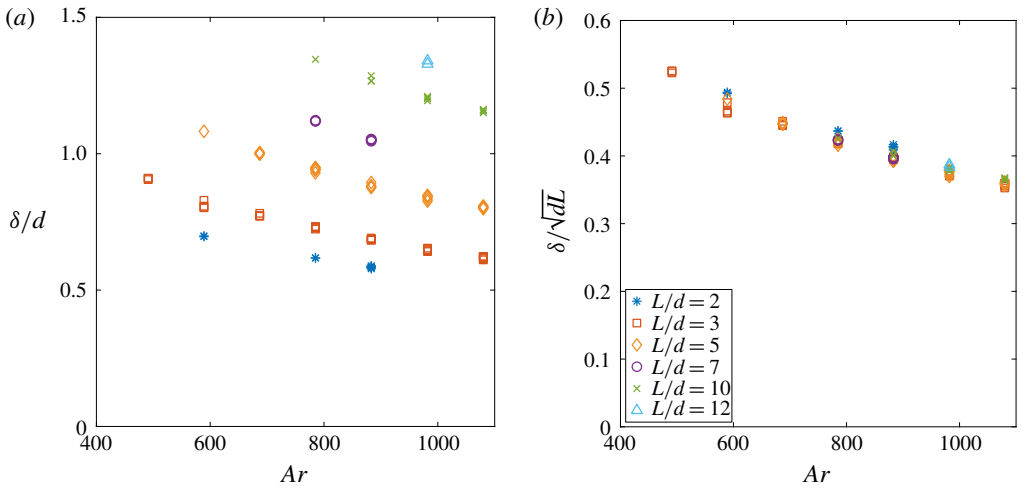

FIGURE 10. (Colour online) Oscillatory viscous wavelength δ versus Ar for various elongation ratios, normalized with (a) the cylinder diameter d; (b) $l_0 = \sqrt{dL}$. Same legend for both panels.

Following this line, the analysis can be pushed ahead by investigating the characteristics of the unsteady boundary layer existing at the surface of a body oscillating in a fluid otherwise at rest at the fluttering frequency $\omega = 2\pi f$. This frequency is much larger than the viscous diffusion frequency ν/d^2 (typically 50 times for $L/d = 2$ and 200 times for $L/d = 10$), so that viscous diffusion of vorticity away from the body surface is strongly limited, the velocity changing sharply to adapt to the no-slip condition. The associated characteristic length scale can be introduced in the form of the oscillatory viscous wavelength, $\delta = 2\pi\sqrt{2\nu/\omega}$. Figure 10($a$) shows that δ is here of the order of the diameter d of the cylinder and depends both on Ar and L/d. Furthermore, figure 10(b) shows that it scales with $l_0 = \sqrt{dL}$, since δ/l_0 is independent of the elongation ratio, within experimental accuracy. This provides a possible physical interpretation for the length scale l_0. Since the effect of the elongation ratio is well captured by the length scale l_0 as well as by the length scale δ, the results presented in figures 9 and 10 can then be expressed in two other forms. The first, illustrated in figure 11(a), is that the Strouhal number based on the thickness δ is independent of the elongation ratio. It displays an evolution with Ar that can be modelled by $1.3Ar^{-0.5}$, leading to the scaling $St^* \simeq 0.11$. The second is that the Reynolds number based on the thickness of the unsteady boundary layer $Re_\delta = u_0\delta/\nu$ is also independent of L/d, as shown in figure 11(b). The result is highlighted by contrasting this figure with figure 6. The dependence on Ar and independence of L/d observed in figure 11(a,b) indicate that, for these quantities, the volume of the body is important as expected (buoyancy being the driving force), yet no longer the exact shape of the body (i.e. its elongation ratio), suggesting a crucial role of the sharp edges of the cylinder (formed where its flat bases join its circular side) in the control of the extension of the unsteady boundary layers created by viscosity in the vicinity of the moving body.

We now turn our attention to the amplitudes of the translational and rotational oscillatory motions of the cylinder. During the fluttering regime, the inclination of the cylinder axis relative to the horizontal, θ, oscillates periodically and regularly, so

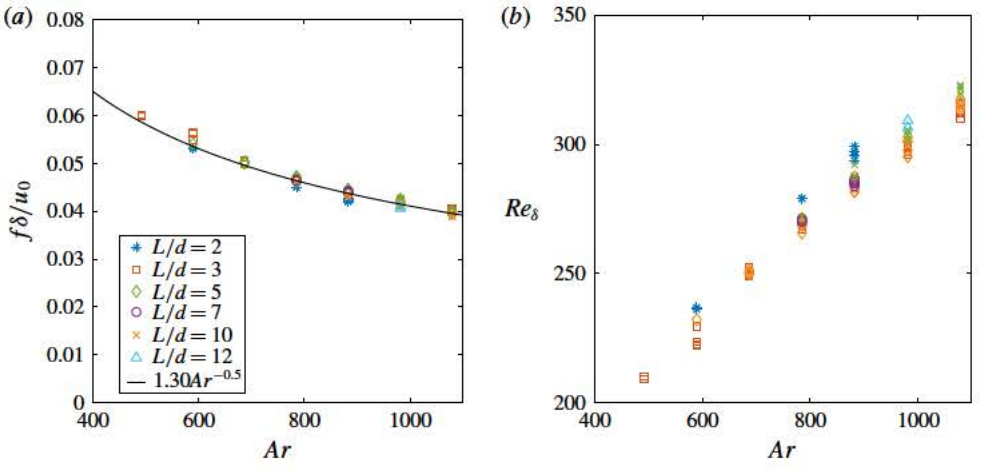

FIGURE 11. (Colour online) (*a*) Strouhal number, $f\delta/u_0$, versus Ar for various elongation ratios, indicating an evolution close to $Ar^{-0.5}$; (*b*) Reynolds number $Re_\delta = u_0\delta/\nu$ based on the Stokes oscillatory wavelength for various elongation ratios as a function of the Archimedes number Ar.

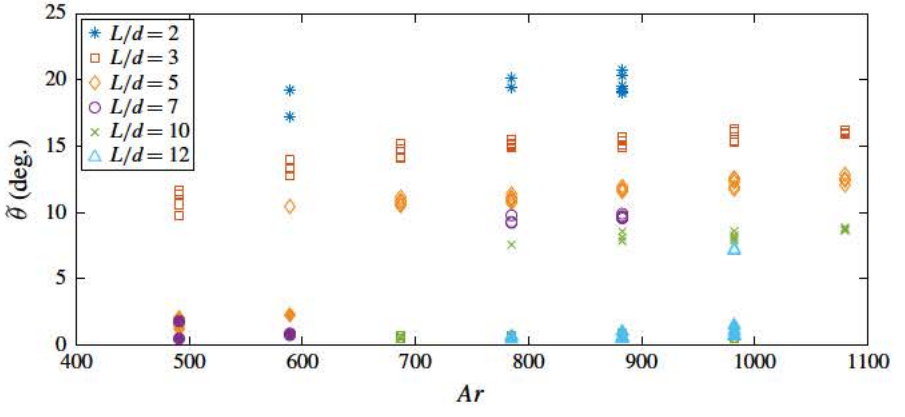

FIGURE 12. (Colour online) Amplitude $\tilde{\theta}$ of the oscillations of θ versus Ar for various elongation ratios for the fluttering and Irregular I regimes. Amplitudes corresponding to the latter regime are plotted using filled markers, except those for $L/d = 10$ which are plotted using ticked boxes. The difference in amplitude between the two regimes is conspicuous.

that it can be modelled by an harmonic function, $\theta = \tilde{\theta}\sin(\omega t - \phi_\theta)$. Figure 12 shows that the amplitude $\tilde{\theta}$ depends both on Ar and L/d, ranging from approximately 20° for $L/d = 2$ to approximately 7° for $L/d = 12$, shorter cylinders displaying a greater oscillation amplitude of their axis. For a given elongation ratio, $\tilde{\theta}$ increases slightly with Ar. A larger increase, of approximately 2.5°, is observed for $L/d = 3$ and Ar going from 490 to 590, which is not observed for higher elongation ratios for the values of Ar that could be explored. For $L/d \geqslant 5$, a jump is in fact observed in a short interval of Ar from the values corresponding to the regime Irregular I, $\tilde{\theta} < 3°$, to those of the fluttering regime, $\tilde{\theta}$ growing further slowly and nearly linearly with Ar.

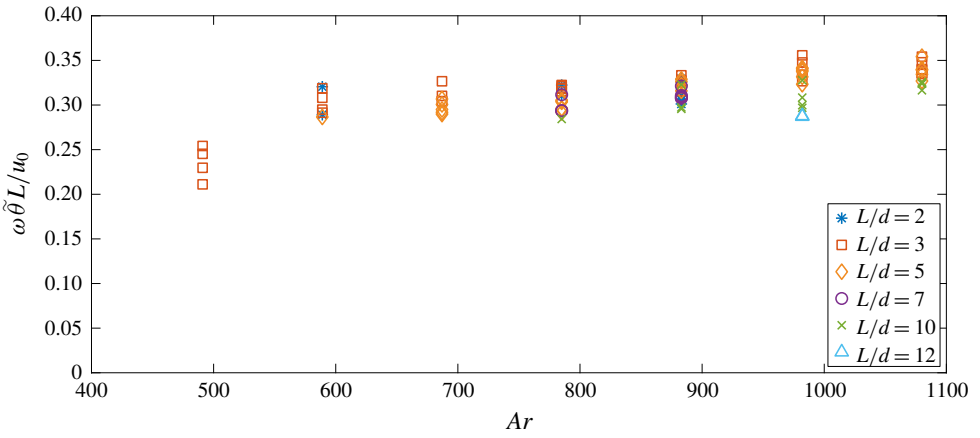

FIGURE 13. (Colour online) Angular velocity of the cylinder $\omega\tilde{\theta}L$ normalized with the gravitational velocity u_0 as a function of the Archimedes number Ar for various L/d.

Chow & Adams (2011) measured $\tilde{\theta}$ in their experiments for freely falling cylinders with $\overline{\rho} \in [1.13, 8.5]$, $L/d \in [1, 90]$ and $Ar \in [200, 6000]$. By considering that the oscillation velocity of the ends of the cylinders is of the same order of magnitude as the mean fall velocity, and that it scales as its excursion over its period, $f_{lit}L\tilde{\theta}$, they propose that $\tilde{\theta}$ is only dependent on the density and elongation ratio, $\tilde{\theta} \sim \sqrt{\overline{\rho}/(L/d)}$. They measured $20^\circ < \tilde{\theta} < 40^\circ$ for $0.3 < \sqrt{\overline{\rho}/(L/d)} < 0.9$. In the present study, $\tilde{\theta}$ cannot be determined using only $\sqrt{\overline{\rho}/(L/d)}$, as it is also dependent on the Archimedes number. Moreover, the amplitude of the oscillations are here significantly smaller than those obtained by Chow & Adams (2011) for similar $\sqrt{\overline{\rho}/(L/d)}$ (ranging here from 0.30 to 0.75).

From the inclination angle of the body, we can determine the rotation rate of the body and its amplitude $\omega\tilde{\theta}$, which is expected to scale with the inertial frequency associated with the mean fall, u_0/L. This scaling is displayed in figure 13, versus the Archimedes number, showing a remarkable gathering of the data points independently of the elongation ratio L/d. Furthermore, the evolution with the Archimedes number is close to a constant, except for $Ar \simeq 500$ at $L/d = 3$, for which the rotation rate is in fact slightly lower, as seen previously for the inclination angle $\tilde{\theta}$.

During the periodic motion, the oscillations of θ are coupled with oscillations of the cylinder centre of gravity. These can be characterized by the component of the body velocity along the cylinder axis, u, which oscillates at the fluttering frequency f, and similarly to θ, can be accurately represented by an harmonic function, $u = \tilde{u}\sin(\omega t - \phi_u)$, $\tilde{u}$ being the oscillation amplitude and ϕ_u the phase. Figure 14 shows that the amplitude $\tilde{u}$ normalized with u_0 ranges between 0.2 and 0.7 for all the cases investigated. For a given elongation ratio, $\tilde{u}/u_0$ increases with Ar. At variance with the amplitude $\tilde{\theta}$, it also increases with L/d. The periodic motion of cylinders with increasing elongation ratios is therefore characterized by stronger axial velocity components and lower inclination angles. The phase difference, $\phi_u - \phi_\theta$, between the oscillations of u and θ is plotted as a function of Ar for various L/d in figure 15. Values remarkably gather along a master curve increasing slightly from approximately $9\pi/8$ to a constant value of approximately $5\pi/4$ for $Ar \geqslant 690$. In the range of parameters considered here, no significant effect of Ar nor of the

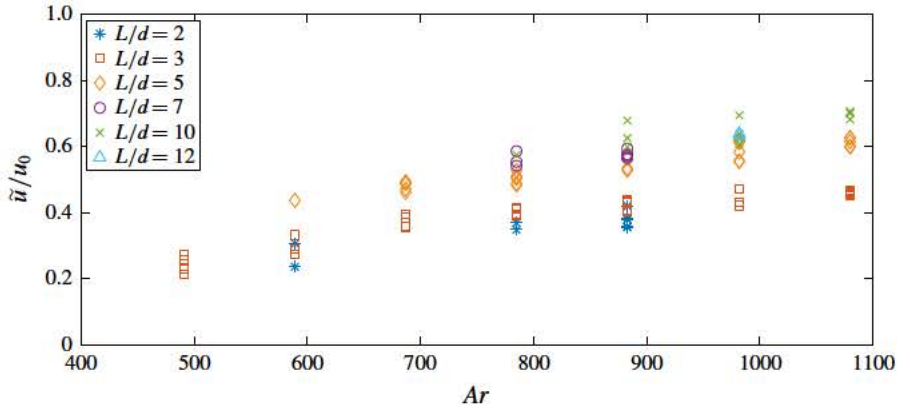

FIGURE 14. (Colour online) Amplitude of oscillation of the velocity component along the cylinder axis, $\tilde{u}$, normalized with u_0 versus Ar for various elongation ratios.

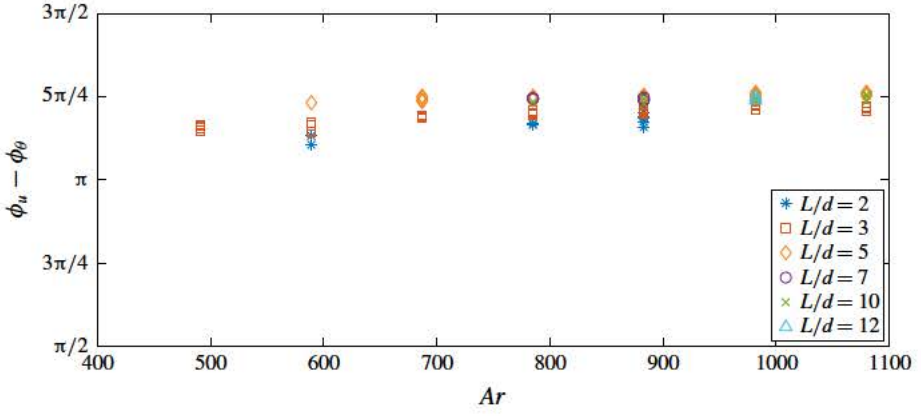

FIGURE 15. (Colour online) Phase difference between the oscillations of u and θ versus Ar for various elongation ratios.

elongation ratio L/d is observed on the phase difference between the oscillations of body inclination and axial velocity, at variance with the results for short-length cylinders (Fernandes *et al.* 2007).

As mentioned in § 2, not all trajectories in the fluttering regime are planar zigzag paths contained in the azimuthal frame. The ellipticity of the path can be characterized by the ratio of $\tilde{w}/\tilde{u}$, $\tilde{w}$ being the amplitude of the oscillations of the velocity component w in the direction perpendicular to the azimuthal plane (see figure 1*c*). This quantity is displayed in figure 16. Mean values of $\tilde{w}/\tilde{u}$ are plotted in the inset of figure 16 versus L/d. The figures indicate that the elongation ratio has a decisive impact on the type of trajectory observed. For long cylinders ($L/d = 7$, 10 and 12), the trajectory is very close to a planar zigzag, with $\tilde{w}/\tilde{u} < 7\,\%$ for all cases. This behaviour changes with decreasing L/d, with $\tilde{w}/\tilde{u} \sim 0.1$ for all cylinders at $L/d = 5$. For $L/d = 3$, we find $\tilde{w}/\tilde{u} \sim 0.2$, and for $L/d = 2$, $\tilde{w}/\tilde{u} \sim 0.3$. A slight increase of $\tilde{w}/\tilde{u}$ with Ar can be seen for $L/d = 3$, even though the data are dispersed due to difficulties in measuring w, which remains small (typically, lower than 1.5 cm s^{-1}).

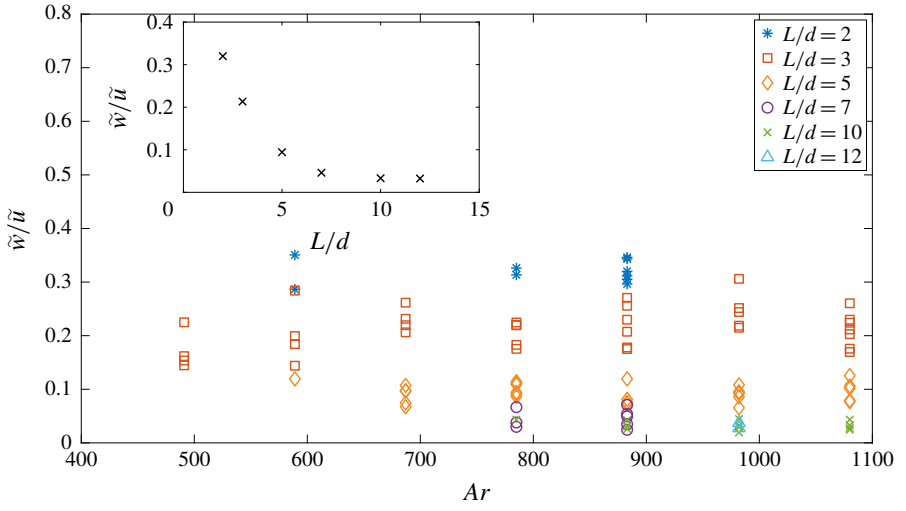

FIGURE 16. (Colour online) Ratio between the amplitude of the oscillations of u and w, versus Ar for various elongation ratios. The inset shows the mean values of $\tilde{w}/\tilde{u}$ for each L/d as a function of L/d.

The body motion gets more complex and three-dimensional as the elongation ratio decreases. The existence of the w component in the fluttering regime is probably related to the existence of oscillations in the azimuthal angle ψ. We were able to detect weak oscillations of ψ of amplitude slightly increasing with Ar, approximately 6° for $L/d = 2$, dispersed between 3° and 7° for $L/d = 3$, lower than 4° for $L/d = 5$ and than 2° for $L/d = 10$. However, the path of shorter cylinders ($L/d = 2$ and 3) could not be fully described, owing to the difficulty in determining properly the phases of w and ψ relative to those of u and θ.

7. Wake visualization and analysis

We now turn our attention to the structure and nature of the wake associated with the various paths observed here for freely falling cylinders. Wake visualization was performed by coating the cylinders in ink before releasing them into the tank. This provides a good qualitative visualization of the wake of the cylinders, as can be seen in figure 17. Several different types of wake are observed in the space of parameters (Ar, L/d) covered here, for cylinders undergoing a rectilinear fall (figure 17*a*,*b*), Irregular III oscillations (figure 17*c*) or strong fluttering (figure 17*d*). In the case of cylinders presenting a rectilinear motion, a comparison can directly be made with the numerical study by Inoue & Sakuragi (2008) for fixed cylinders with finite lengths and free ends.

We observe a single case of steady wake for $Ar = 200$ and $L/d = 3$, corresponding to $Re_d = 120$ and to the lightest cylinder tested in our experiment which displays a rectilinear fall (see figure 17*a*). This wake is characterized by the formation of four longitudinal dye streaks, alike the steady wake observed numerically by Inoue & Sakuragi (2008) for $Re_d = 150$ and $L/d = 1$ (denoted Type IV in their work) and composed of two pairs of counter-rotating longitudinal vortices (see their figures 5*b* and 6). To our knowledge, this is the first experimental evidence of the existence of the wake structure uncovered numerically by Inoue & Sakuragi (2008)

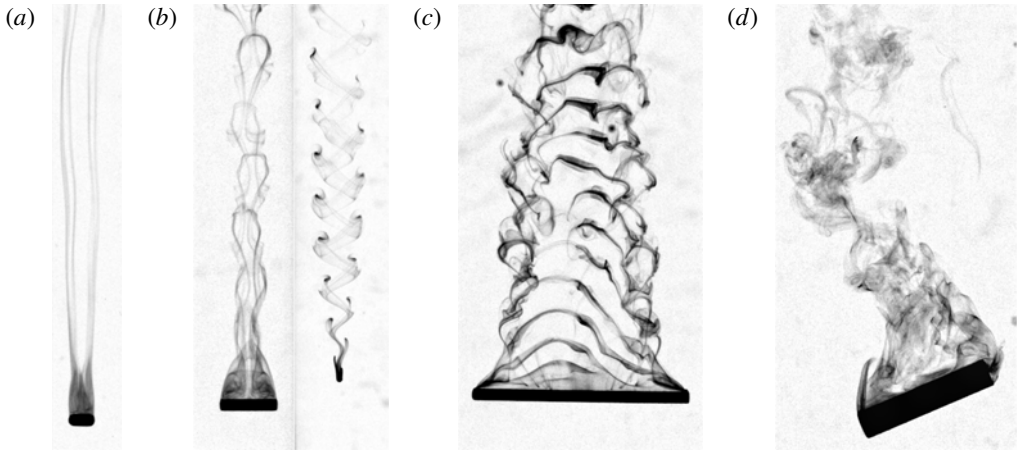

FIGURE 17. Different types of wake observed. (*a*) Steady wake with two pairs of longitudinal vortices observed for a cylinder in rectilinear motion with ($Ar = 200, L/d = 3$). (*b*) Periodic release of hairpin vortices observed for cylinders following rectilinear paths with ($Ar = 200, L/d = 5$) on the left and ($Ar = 200, L/d = 10$) on the right. (*c*) Wake for long cylinders ($Ar = 600, L/d = 20$) displaying weak azimuthal oscillations. (*d*) Fluttering regime ($Ar = 1100, L/d = 5$).

for cylinders with slightly different parameters, and corresponding to the shedding of two steady counter-rotating vortex pairs behind the cylinder.

For $Ar = 200$, $L/d = 5$ and 10 (corresponding to $Re_d = 80$ and 50 respectively), we observe a periodic double-sided shedding of hairpin vortices (figure 17*b*). It should be noted that in both cases, no significant horizontal displacement of the body was detected. The vortex shedding frequency was estimated to be approximately 7 Hz. Inoue & Sakuragi (2008) observed similar shedding of vortices for $Re_d = 150$ and $L/d = 5$, for $Re_d = 100$ and $L/d = 10$, and for $Re_d = 60$ and $L/d = 13$, referenced as Type III (see their figure 5*a*). This type of wake is, according to Inoue & Sakuragi (2008), characterized by disconnected hairpin-shaped vortices shed alternatively from opposite sides of the curved surface of the cylinder, in contrast to vortices shed in Types I and II, to be discussed hereafter. An experimental illustration of a similar wake is also provided by Jayaweera & Mason (1965) for $Re_d = 70$ and $L/d = 10$.

Figure 17(*c*) shows the wake of a cylinder with $Ar \simeq 600$ and $L/d = 20$ ($Re_d \simeq 130$) corresponding to regime Irregular III. The wake for this freely moving long cylinder can be compared to the observations for fixed long cylinders with free ends from the numerical study by Inoue & Sakuragi (2008) and without free ends from the experimental results by Williamson (1989). The instantaneous structure of the wake observed in this case is similar to that referred to as Type II by Inoue & Sakuragi (2008), and as oblique vortex shedding by Williamson (1989). However, the cylinder shown in figure 17(*c*) presents weak regular azimuthal oscillations, which are coupled to the wake. A periodic beating of the wake is in fact observed here near the ends of the cylinder, at the oscillation frequency of the azimuthal angle ψ.

In the case of fluttering cylinders, the coupling between the wake and the motion of the body leads to a significantly different wake structure, strongly influenced by the orientation of the body and of its flat faces relative to its velocity. An example is shown on figure 17(*d*) for $Ar \simeq 1100$ and $L/d = 5$ ($Re_d \simeq 585$) for a body displaying a fluttering motion of amplitude $\theta \simeq 12°$.

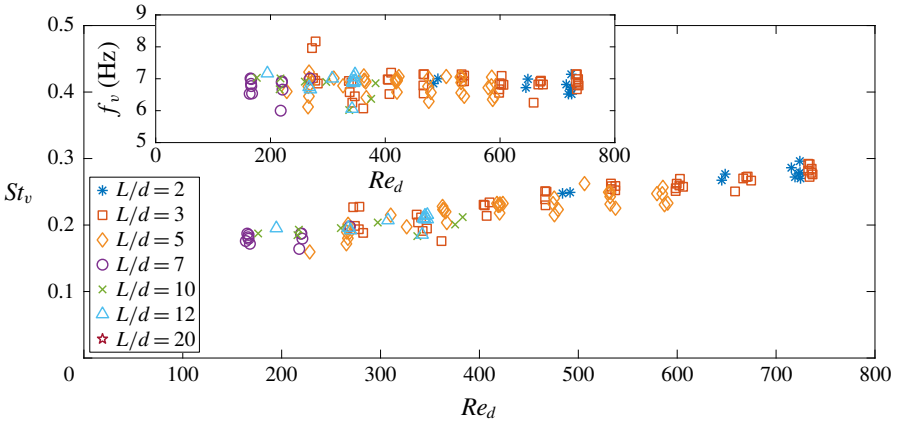

FIGURE 18. (Colour online) Strouhal number based on the high-frequency vertical oscillation of v, $St_v = f_v d/\overline{u_Z}$, versus the Reynolds number.

Flow visualization thus revealed that an unsteady wake is observed even for bodies maintaining a rectilinear motion. A deeper analysis of the cylinder kinematics was therefore carried out in order to uncover possible effects of the wake unsteadiness in their path. This revealed that high-frequency oscillations of the vertical velocity of the cylinder (which can be seen on v, as $v \simeq u_Z$ for all cases) are observed on most cylinders recorded with an acquisition frequency of 50 Hz. These oscillations occur at a frequency $f_v \sim 7$ Hz measured by the spectral analysis of v (figure 18), and are observed for cylinders presenting rectilinear as well as fluttering paths. The amplitude of this vertical oscillation is very low, less than 4 % of $\overline{u_Z}$ for all cases, and was difficult to measure accurately. f_v is remarkably constant with Re_d, with 6 Hz $< f_v <$ 7.2 Hz for all cases but 2, being at approximately 8 Hz. No effect of L/d was detected on f_v. Vortex shedding from the curved side of the cylinder is a plausible cause for these oscillations, as they occur for all cylinders independently of their path, L/d and Re_d. Furthermore, this frequency is close to the estimated vortex shedding frequency from wake visualization videos for instance for $Re_d = 50$ and $L/d = 10$ (figure 17*b*).

A corresponding Strouhal number can be built as $St_v = f_v d/\overline{u_Z}$. St_v increases with Re_d and ranges from approximately 0.16 to 0.30 (figure 18). The elongation ratio has seemingly no impact on St_v in the range explored. Comparison of St_v with previous results of the literature can be seen in figure 19. Williamson & Brown (1998) proposed a fit in series of $Re_d^{-1/2}$ for the Strouhal number corresponding to the Bénard–von Kármán instability about a fixed cylinder, $St_{BvK} = 0.2731 - 1.1129 Re_d^{-1/2} + 0.4821 Re_d^{-1}$ for $Re_d \leqslant 1000$. For approximately $160 < Re_d < 400$ corresponding to rectilinear and Irregular I paths (figure 7), the present results for St_v are in good agreement with this expression. The Strouhal number values, computed by Inoue & Sakuragi (2008) for fixed cylinders with free ends at $Re_d = 100$, are also plotted in figure 19. They are significantly smaller than the results for infinite cylinders, ranging from approximately 0.08 for $L/d \simeq 3$ to 0.13 for $L/d \simeq 20$. Qu *et al.* (2013) and Gioria *et al.* (2011) performed numerical studies of the flow past a cylinder using domains of varying spanwise length. Although measuring St_{BvK} was not the primary aim of their work, they provided values of St_{BvK} for some Reynolds numbers. Qu *et al.* (2013) studied cylinders of spanwise length $L = 10d$ and $12d$ at $Re_d = 200$ providing

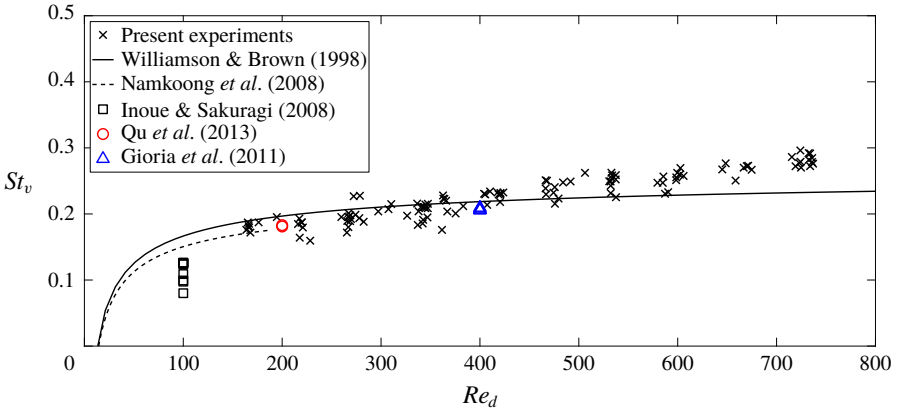

FIGURE 19. (Colour online) Strouhal number based on the high-frequency vertical oscillation of v, $St_v = f_v d/\overline{u_Z}$, versus Re_d, comparison with results from Williamson & Brown (1998), Qu *et al.* (2013), Gioria *et al.* (2011). The dashed line corresponds to the expression $St_v = 0.2429 - 0.9238 Re_d^{-1/2}$ from Namkoong *et al.* (2008).

$St_{BvK} \simeq 0.18$, and Gioria *et al.* (2011) cylinders of spanwise length $L = 6d$ and $12d$ at $Re_d = 400$ yielding $St_{BvK} \simeq 0.21$. Both St_{BvK} values are in good agreement with the present experimental results. It should be noted that Qu *et al.* (2013) also performed numerical simulations for infinite cylinders, and that the values of St_{BvK} they found were in remarkable agreement with the model of Williamson & Brown (1998). For the same Re_d, the Strouhal number values they computed were thus lower for cylinders of fixed spanwise length. Finally, it can be pointed out that Namkoong *et al.* (2008) observed numerically that for $66 < Re_d < 185$ the degrees of freedom in rotation and translation of an infinitely long (i.e. two-dimensional) cylinder lead to a slight decrease in the frequency of vortex shedding and of the associated oscillatory motion of the cylinder, with typically $St_{BvK} \simeq 0.17$ for $\overline{\rho} = 1.01$ and $Re_d = 156$, corresponding to the trend observed here for lower Re_d (figure 19). For Re_d larger than approximately 400, corresponding to cylinders displaying in our configuration a fluttering motion (figure 7), we find values for the Strouhal number St_v higher than those of St_{BvK}. The high-frequency mode is therefore observed to coexist, and most possibly is coupled, with the fluttering mode, as oscillations of v at f_v are detected to be superimposed to those at twice the fluttering frequency.

The correspondence between the Strouhal numbers provided by the oscillations of v measured in our experiments, by the wake visualizations and by various numerical and experimental data on vortex shedding in the wake of fixed cylinders suggests that vortex shedding from the curved side of the cylinder may be responsible for the weak oscillations of the vertical velocity observed here for freely falling cylinders. An associated rotation of the cylinder about its axis could possibly exist along with the high-frequency vertical oscillation of the body, as observed by Namkoong *et al.* (2008). In our experiments, no such motion could be detected across all experiments outside the transient period following the release of the body from rest. However, the measurement method for the rotation is not accurate enough to determine such low-amplitude motions (rotational and translational oscillations with amplitudes, respectively, of approximately 0.7° and $0.1d$ for $\overline{\rho} = 1.01$ and $Re_d = 156$ in the simulations by Namkoong *et al.* (2008) for freely falling two-dimensional cylinders).

Numerical simulation may be a more adapted and accurate tool to carry further the investigation of the different regimes of low-amplitude oscillations of the cylinders.

8. Conclusion

We investigated the motion of freely falling elongated cylinders (length-to-diameter ratio ranging from 2 to 20) in a liquid otherwise at rest, for the density ratio $\overline{\rho} \simeq 1.16$ and for Archimedes numbers ranging from 200 to 1100. The Archimedes numbers are based on the body equivalent diameter, enabling us to investigate, at given Ar, and therefore at given volume of the body and given buoyancy force ($\overline{\rho}$ being fixed), the effect of the elongation ratios of the cylinders on their behaviour. A shadowgraphy technique involving two cameras and two backlights mounted on a travelling cart was used to track the cylinders along their fall. A dedicated image processing algorithm was further implemented to properly reconstruct the position and orientation of the cylinder in the 3-D space. In the range of parameters explored, we identified three main types of path, matching regimes known to exist for three-dimensional bodies (disks and spheres). Two of these are stationary, the rectilinear motion and the large-amplitude oscillatory motion (also referred to as fluttering or zigzag motion). The third one comprises irregular oscillatory motions of low amplitude (denoted here Irregular I to III) that may be assimilated to A-regimes or quasi-vertical regimes of the literature (see for instance Ern *et al.* 2012). The rectilinear motion observed here is twofold. On the one hand, a steady vertical fall associated with a steady wake composed by two pairs of longitudinal vortices generated behind the cylinder is observed (here, only for $Ar = 200$ and $L/d = 3$). On the other hand, a vertical rectilinear motion with very light vertical oscillations at a Strouhal number St_v (frequency f_v) close to that of the Bénard–von Kármán instability is observed in association with an unsteady wake, displaying in some range of parameters a periodic shedding of hairpin vortices. No additional motion of the body could be detected here experimentally, but horizontal or rotational motions of the body could possibly occur for these bodies. Their path would then belong to the second class of paths identified here, the low-amplitude rotational oscillatory regimes. The low-amplitude rotational regimes observed here present oscillations of irregular amplitude, that are difficult to disentangle from noise. Nevertheless, we tried to grasp some distinctive features and classified them in three groups. Irregular III corresponds to oscillations essentially of the azimuthal angle ψ of the cylinder at Strouhal numbers about St_v for long cylinders ($L/d = 20$). Irregular I and Irregular II present irregular oscillations of the inclination angle θ and of the body centre of gravity position at a frequency close to the fluttering frequency f, that stay weak (lower than 3°) over the whole time sequence (Irregular I) or are low-frequency modulated (Irregular II), amplitudes varying in this case from less than 3° to sometimes approximately 10°. These salient features are proposed here as a basis for future developments and improved analysis of these paths, as it must be stressed that experimentation, at least the one carried out here, is not accurate enough to elaborate a full characterization of these complex paths. Interestingly, though no significant oscillatory motion of the cylinder is clearly visible in these regimes, a significant agitation due to wake unsteadiness is present in the liquid, featuring in particular three-dimensional vortex shedding. A sharp distinction between these regimes and the fluttering regime is conspicuous, for large-amplitude oscillations in both orientation and translation of the body are manifest in the latter. In the fluttering regime, the rotation of the body as well as its tendency to slide along its symmetry axis are strongly coupled with an unsteady wake that has a

distinct outline, and whose characteristic features are related to the fact that the flat sides of the cylinder contoured by sharp edges tend now to face the direction of motion. Still, closer examination of the temporal signals of the body vertical motion revealed coexistence in the fluttering regime of oscillations at frequencies $2f$ (fluttering behaviour) and f_v, suggesting a complex shedding of vortices originating both from the curved side of the cylinder and from the flat faces.

The detailed analysis of the body kinematics in the fluttering regime brought to light a series of remarkable properties of this motion. In the range of parameters Ar and L/d investigated here for $\overline{\rho} \simeq 1.16$, the values of the mean vertical velocity of the body gather together into the relation $\overline{u_Z} \simeq 1.46u_0$, where $u_0 = ((\overline{\rho} - 1)gd)^{1/2}$ is the gravitational velocity based on the cylinder diameter d. The mean fall velocity of the cylinder appears therefore independent of its length, depending solely on its diameter, in the same way the mean velocity of the finite-length disk is independent of its diameter, depending solely on its length or thickness (see for instance Fernandes *et al.* 2007, where $u_0 = (|\overline{\rho} - 1|gL)^{1/2}$, $\overline{\rho} \simeq 0.99$ and $0.1 \leqslant L/d \leqslant 0.5$). Proceeding along with this parallel, a unified view of the fluttering frequency f of finite-length cylinders (either short or elongated) with density ratios close to unity is provided by the Strouhal number,

$$St^* = fl_0/u_0 \quad \text{with } l_0 = \sqrt{dL}, \tag{8.1}$$

featuring the length scale l_0 and the gravitational velocity scale based on the dimension of the cylinder corresponding to the direction of its mean vertical motion (the length for a short-length cylinder and the diameter for an elongated cylinder), yielding $St^* \simeq 0.11$ for elongated cylinders, and $St^* \simeq 0.1$ for disks in Fernandes *et al.* (2007). These results bring to the fore that the characteristic length and velocity scales of the body motion are respectively l_0 and u_0. When made dimensionless using these scales, the mean vertical velocity and the frequency of the oscillations are almost independent of L/d and Ar. Their relevance is further intensified by considering that the Archimedes number defined using the equivalent diameter of the cylinder D as mentioned previously, can be expressed as the Reynolds number built with u_0 and l_0, $Ar = \sqrt{3/2}u_0 l_0/\nu$.

Moving beyond this point to improve our understanding is not an easy task with the results at hand. The scaling proposed for the fluttering frequency appears as purely inertial, based on the inertial time scale l_0/u_0. However, primary causes of frequency selection could lie deeper in the flow organization in the vicinity of the body due to the effect of viscosity. The fluttering period is an order of magnitude shorter than the viscous diffusion time scale d^2/ν, so that the liquid velocity changes sharply to satisfy the no-slip condition on the cylinder surface and viscous effects are responsible for flow reversal in the vicinity of the cylinder. The extension of the recirculation region can be estimated with the oscillatory viscous wavelength, $\delta = 2\pi\sqrt{2\nu/\omega}$, which scales with $l_0 = \sqrt{dL}$, since δ/l_0 is found to be, within experimental accuracy, independent of the elongation ratio for given Ar. We therefore suggest that the origin of the length scale l_0 is related to viscosity, as a characteristic recirculation length scale. For the unsteady boundary layers at rather high frequencies involved here, flow reversal might be expected to occur simultaneously both on the face and side of the cylinder surface, coupling therefore the two characteristic dimensions of the body, d and L.

We further explored the characteristics of the amplitudes of oscillation in translation and rotation of the body and showed that cylinders with higher elongation ratios display a higher axial velocity component u and lower inclination angle θ. The

rotation rate of the cylinders scales with the inertial frequency scale, u_0/L, depending only slightly on Ar and L/d. One of the most remarkable results is however provided by the phase difference $(\phi_u - \phi_\theta)$ between the oscillations of u and θ, which increases slightly from approximately $9\pi/8$ to a constant value of $5\pi/4$ for larger Ar, whatever the elongation ratio L/d. This result is markedly at variance with the behaviour of disks, where a strong influence of the disk aspect ratio on the phase difference is observed, changing by approximately $\pi/2$ when L/d varies between 0.1 and 0.5 (Fernandes *et al.* 2007). In spite of these properties, it is worth pointing out that the path of the cylinders remains complex. The fluttering motion is moderately three-dimensional (ellipticity lower than 0.3), becoming more planar as the elongation ratio of the body increases, tending towards a path contained in the plane formed by the body symmetry axis and the vertical. Since the motion in the perpendicular direction to this plane is weak, its characterization requires a specific investigation, which is beyond the scope of the present paper.

Acknowledgements

The authors are grateful to S. Cazin, G. Ehses and R. Soeparno for the technical support provided for the experiments. They also gratefully acknowledge financial support by IFP Energies Nouvelles, Solaize, France and warmly thank D. Ferré and R. Brahem (from department R1240S), C. P. da Fonte and L. Gamet (R1510S), as well as J. L. Pierson (R04) for their interest in the problem.

Appendix. Three-dimensional reconstruction of a cylinder using its projected contour

When observing a 3-D object through a camera using shadowgraphy, only the 2-D projection of its contour is seen. This projected contour loses some properties of the 3-D object, such as symmetries. In our study, we need to determine accurately the pose, i.e. the accurate position in a 3-D space, of the cylinders. In the case of a cylinder, the projected contour on the camera plane loses the planar symmetry property of the cylinder. Moreover, the distortion is not even for all contour points, and the ones further from the camera axis are more distorted. As a result, the shape and orientation of the projected cylinder contour are vastly different from its physical ones. Furthermore, no contour point is easily matchable to a physical point of the cylinder. In consequence, determining the exact features of the 3-D object using solely its projection is not a trivial matter. The 3-D reconstruction (also called pose estimation) of a cylinder using its projected contour is a problem investigated by several computer vision studies due to its difficulty and numerous applications (Huang *et al.* 1996; Doignon & de Mathelin 2007; Shiu & Huang 1993; Navab & Appel 2006). Huang *et al.* (1996) presented a pose determination method using only the straight line projection of the sides of the cylinder, based on the image from a single camera. Being based on a geometric transformation, it can be implemented directly on the cylinder contour (versus on the images, which is computationally heavier) and runs fast. Consequently, the method of Huang *et al.* (1996) was chosen in the present work to solve the problem of the 3-D reconstruction of the cylinder.

As mentioned before, the perspective distortion of a cylinder depends on its position in the camera field of view. Features of the cylinder can only be accurately extracted when its axis is perfectly orthogonal to the camera optical axis. In our experiments, the rotation and fall velocity of the cylinder made it impossible to keep it in that configuration at all times. Additionally, the projected contour of the cylinder only has

smooth surfaces, and no angular point can be identified and matched to a physical point of the cylinder. Therefore, other geometric properties of the cylinder contour that can be easily identified have to be found. Huang *et al.* (1996) chose to use the projection of the straight sides of the cylinder as such features. Once the contour points belonging to the cylinder straight sides have been properly identified, it is possible to determine the equation of the two planes containing each the centre of projection of the camera and one of these lines. Then, a new image plane, called the canonical image plane, is created. The cylinder contour points in this new plane correspond to what would have appeared on the original image plane if the cylinder axis had been orthogonal to the camera optical axis. Specific features of cylinder contour in the canonical image plane can be used to determine the position and orientation of the cylinder in the laboratory frame. Once these points have been identified, they are located in the original image plane using the inverse projection transformation to the one used to go from the original image plane to the canonical one. Then, their positions in the laboratory frame are deduced from the camera calibration. The output from this method is the centre of the two flat faces of the cylinder.

The method described in Huang *et al.* (1996) was developed to be used with a single camera. In our experimental set-up, we have two orthogonal cameras. Given the nature of a camera, the method of Huang *et al.* (1996) is very accurate to determine the two coordinates corresponding to its image plane, but less so for the third one, corresponding to its depth of field. In the present work, the method of Huang *et al.* (1996) was adapted so that for each frame, a camera was used to give the two coordinates corresponding to its image plane, and the remaining coordinate was given by the other camera. The camera outputting two coordinates was chosen to be the one having the best view angle of the cylinder. This adaptation proved to increase significantly the accuracy of the reconstruction method.

Given the vast number of operations involved in the method of Huang *et al.* (1996), it is difficult to estimate quantitatively its accuracy. Huang *et al.* (1996) suggest to use the computed cylinder length, deduced from the coordinates of the two flat faces of the cylinder, and to compare it to the actual cylinder length to have an estimation of the accuracy. All the data we provide in this work have an associated mean relative error of 4.5 % for the length, with a maximum error of 10 % and a root-mean-square value of 4 %. When the error was greater than 10 %, the data were discarded. This occurred in 22 out of 248 runs.

REFERENCES

ANDERSEN, A., PESAVENTO, U. & WANG, Z. J. 2005*a* Analysis of transitions between fluttering, tumbling and steady descent of falling cards. *J. Fluid Mech.* **541**, 91–104.

ANDERSEN, A., PESAVENTO, U. & WANG, Z. J. 2005*b* Unsteady aerodynamics of fluttering and tumbling plates. *J. Fluid Mech.* **541**, 65–90.

AUGUSTE, F. & MAGNAUDET, J. 2018 Path oscillations and enhanced drag of light rising spheres. *J. Fluid Mech.* **841**, 228–266.

AUGUSTE, F., MAGNAUDET, J. & FABRE, D. 2013 Falling styles of disks. *J. Fluid Mech.* **719**, 388–405.

BELMONTE, A., EISENBERG, H. & MOSES, E. 1998 From flutter to tumble: inertial drag and Froude similarity in falling paper. *Phys. Rev. Lett.* **81** (2), 345–348.

CHOW, A. C. & ADAMS, E. E. 2011 Prediction of drag coefficient and secondary motion of free-falling rigid cylindrical particles with and without curvature at moderate Reynolds number. *J. Hydraul. Engng* **137** (11), 1406–1414.

CHRUST, M., BOUCHET, G. & DUŠEK, J. 2013 Numerical simulation of the dynamics of freely falling discs. *Phys. Fluids* **25**, 044102.

DAUCHY, C., DUŠEK, J. & FRAUNIÉ, P. 1997 Primary and secondary instabilities in the wake of a cylinder with free ends. *J. Fluid Mech.* **332**, 295–339.

DOIGNON, C. & DE MATHELIN, M. 2007 A degenerate conic-based method for a direct fitting and 3-D pose of cylinders with a single perspective view. In *Proceedings of the 2007 IEEE International Conference on Robotics and Automation*, pp. 4220–4225. IEEE.

ERN, P., RISSO, F., FABRE, D. & MAGNAUDET, J. 2012 Wake-induced oscillatory paths of bodies freely rising or falling in fluids. *Annu. Rev. Fluid Mech.* **44**, 97–121.

FERNANDES, P. C., ERN, P., RISSO, F. & MAGNAUDET, J. 2008 Dynamics of axisymmetric bodies rising along a zigzag path. *J. Fluid Mech.* **606**, 209–223.

FERNANDES, P. C., RISSO, F., ERN, P. & MAGNAUDET, J. 2007 Oscillatory motion and wake instability of freely rising axisymmetric bodies. *J. Fluid Mech.* **573**, 479–502.

GIORIA, R. S., MENEGHINI, J. R., ARANHA, J. A. P., BARBEIRO, I. C. & CARMO, B. S. 2011 Effect of the domain spanwise periodic length on the flow around a circular cylinder. *J. Fluids Struct.* **27** (5), 792–797.

HOROWITZ, M. & WILLIAMSON, C. H. K. 2006 Dynamics of a rising and falling cylinder. *J. Fluids Struct.* **22**, 837–843.

HOROWITZ, M. & WILLIAMSON, C. H. K. 2010 Vortex-induced vibration of a rising and falling cylinder. *J. Fluid Mech.* **662**, 352–383.

HUANG, J. B., CHEN, Z. & CHIA, T. L. 1996 Pose determination of a cylinder using reprojection transformation. *Pattern Recogn. Lett.* **17** (10), 1089–1099.

INOUE, O. & SAKURAGI, A. 2008 Vortex shedding from a circular cylinder of finite length at low Reynolds numbers. *Phys. Fluids* **20** (3), 033601.

JAYAWEERA, K. O. L. F. & MASON, B. J. 1965 The behaviour of freely falling cylinders and cones in a viscous fluid. *J. Fluid Mech.* **22** (4), 709–720.

LAMB, H. 1993 *Hydrodynamics*. Cambridge University Press.

MARCHILDON, E. K., CLAMEN, A. & GAUVIN, W. H. 1964 Drag and oscillatory motion of freely falling cylindrical particles. *Can. J. Chem. Engng* **42** (4), 178–182.

MATHAI, V., ZHU, X., SUN, C. & LOHSE, D. 2017 Mass and moment of inertia govern the transition in the dynamics and wakes of freely rising and falling cylinders. *Phys. Rev. Lett.* **119**, 054501.

NAMKOONG, K., YOO, J. Y. & CHOI, H. G. 2008 Numerical analysis of two-dimensional motion of a freely falling circular cylinder in an infinite fluid. *J. Fluid Mech.* **604**, 33–54.

NAVAB, N. & APPEL, M. 2006 Canonical representation and multi-view geometry of cylinders. *Intl J. Comput. Vis.* **70** (2), 133–149.

PROVANSAL, M., SCHOUVEILER, L. & LEWEKE, T. 2004 From the double vortex street behind a cylinder to the wake of a sphere. *Eur. J. Mech. (*B*/Fluids)* **23**, 65.

QU, L., NORBERG, C., DAVIDSON, L., PENG, S.-H. & WANG, F. 2013 Quantitative numerical analysis of flow past a circular cylinder at Reynolds number between 50 and 200. *J. Fluids Struct.* **39**, 347–370.

ROMERO-GOMEZ, P. & RICHMOND, M. C. 2016 Numerical simulation of circular cylinders in free-fall. *J. Fluids Struct.* **61**, 154–167.

SCHOUVEILER, L. & PROVANSAL, M. 2001 Periodic wakes of low aspect ratio cylinders with free hemispherical ends. *J. Fluids Struct.* **15**, 565.

SHIU, Y. C. & HUANG, C. 1993 Pose determination of circular cylinders using elliptical and side projections. In *IEEE 1991 International Conference on Systems Engineering*, pp. 265–268. IEEE.

TCHOUFAG, J., FABRE, D. & MAGNAUDET, J. 2014 Global linear stability analysis of the wake and path of buoyancy-driven disks and thin cylinders. *J. Fluid Mech.* **740**, 278–311.

VAKIL, A. & GREEN, S. I. 2009 Drag and lift coefficients of inclined finite circular cylinders at moderate Reynolds numbers. *Comput. Fluids* **38**, 1771–1781.

WILLIAMSON, C. H. K. 1989 Oblique and parallel modes of vortex shedding in the wake of a circular cylinder at low Reynolds numbers. *J. Fluid Mech.* **206**, 579–627.

WILLIAMSON, C. H. K. 1996 Vortex dynamics in the cylinder wake. *Annu. Rev. Fluid Mech.* **28**, 477–539.

WILLIAMSON, C. H. K. & BROWN, G. L. 1998 A series in $1/\sqrt{Re}$ to represent the Strouhal–Reynolds number relationship of the cylinder wake. *J. Fluids Struct.* **12** (8), 1073–1085.

WILLIAMSON, C. H. K. & GOVARDHAN, R. 2004 Vortex-induced vibrations. *Annu. Rev. Fluid Mech.* **36**, 413–455.